

Transition radiation detectors

Boris Dolgoshein

Moscow Institute of Physics and Engineering, Moscow, Russian Federation

Received 19 July 1992

The use of transition radiation (TR) as a means of identifying high energy particles has now become a subject of intensive experimental investigations and applications. Our intention is first to study the physics of these phenomena and to describe ways of building detectors which can efficiently identify particles.

1. Introduction

The existence of transition radiation was predicted in 1946 by Ginzburg and Frank [1]. The radiation is emitted when a particle moves across the interface of two media with different dielectric constants. The radiation which is predicted directly from the equation of electrodynamics, however, was not studied experimentally for a long time because the expected number of quanta was extremely small. After the first observation of the transition radiation in the optical region [2], many early studies indicated that the application of the optical transition radiation for the detection and identification of individual particles seemed to be severely limited due to the inherent low intensity of the radiation [3,4].

Interest in transition radiation was renewed when Garibian [5,6] showed that the radiation should also appear in the X-ray region for ultrarelativistic particles. His theory predicted some remarkable features for transition radiation in the X-ray region. First, the total energy loss by a charged particle should be proportional to the Lorentz factor of the particle, γ ($\gamma = E/mc^2$). This is quite attractive for determining the energy of the particles because some of the known methods of detection become marginal at high values of γ , e.g., the method using a Cherenkov radiation detector. Second, as in any other source of radiation from relativistic particles, the radiation is extremely forward peaked within an angle of order $1/\gamma$. This fact could make the detection of transition radiation complicated by the necessity of separating the charged particles from the radiation. Third, the electrodynamic nature of the radiation indicates that in an interface between two different dielectric media, the number of photons per particle is of order $\alpha = 1/137$. Nevertheless, by using a multilayered dielectric radiator spaced in vacuum, it is possible to increase the radiation yield

cumulatively. The minimum space required between the layers is proportional to the radiation wavelength and is therefore shorter for radiation in the X-ray region than in the optical region.

Immediately, the prediction of the X-ray transition radiation attracted attention of the experimentalists. The works of the Soviet physicists [7–13] and of Yuan and collaborators [14–16] using beams of high energy electrons provided the evidence for the existence of transition radiation in both the optical and X-ray regions. The purpose of these experiments was to determine γ of a single particle by using a combination of multilayered radiators and specifically designed X-ray detectors. The detectors were mainly solid state counters, streamer chambers, and sodium iodide scintillators [12–14]. In due course, proportional chambers (PC) were introduced as more convenient X-ray detectors [16,17]. In spite of these very extensive works, it was still a marginal radiation and physicists were not convinced that transition radiation would be useful for the identification of ultrarelativistic particles.

However, beginning with the work [18,19], where the TRD (CH₂ or Li foils as radiation + PC) was used for identification of electrons in cosmic rays and in an ISR experiment, transition radiation detector became a powerful tool for identification of high energy particles. We have now enough information necessary to design transition radiation detectors for different experimental situations.

Section 2 reviews the fundamental formulas of transition radiation theory primarily established by Soviet physicists. Both a qualitative and a quantitative analysis of the theoretical formulas are given. Some computational methods to determine the radiation yields are developed. Section 3 discusses the experimental methods on how to detect transition X-rays and how to identify particles with the detected signals. Section 4 contains the results of optimization of the TRD struc-

ture; section 5 presents the applications of TR detectors for different experimental situations and section 6 discusses the possibilities and limitations of TRD for the next generation of high luminosity colliders.

2. Theoretical description of TR

2.1. General features

The radiation from a uniformly moving charge in a medium with a variable dielectric constant is analogous to the radiation from a particle moving non-uniformly. In both cases the radiation is related to the phase velocity of the electromagnetic waves in the given medium and the velocity of the charged particle. The difference is that in the former case the phase velocity of the wave changes, while in the latter particle velocity changes. (In this sense, TR and bremsstrahlung have the same origin.)

As an extreme case of the phenomenon, assume that a nonrelativistic particle enters a metal from vacuum. The TR is identical with the bremsstrahlung spectrum because the particle is brought to a complete stop at the surface of the metal. In this case the TR results from the annihilation of the dipole formed by an electron and its image charge on the surface of the material with a different dielectric constant. For a charge e moving at a constant velocity v normal to the surface, the energy radiated into solid angle $d\Omega$ at an angle θ to the trajectory of the particle is given by [20]

$$\frac{d^2W}{d\omega d\Omega} = \frac{e^2 v^2}{\pi^2 c^3} \sin^2 \theta \quad (1)$$

in a bandwidth of frequency $d\omega$. The angular distribution of the radiation is the same as for a dipole placed on the surface. The radiation intensity is proportional to v^2 . Therefore, the radiation is the same as when the particle would go into vacuum from a metal.

For the dielectric material in the relativistic case, a more general formulation is obtained and results of this formulation are given in many theoretical papers [6,21,22]. At the boundary of two different media with dielectric constants ϵ_1 and ϵ_2 ($\mu_1 = \mu_2 = 0$ is assumed) a charged particle with constant velocity v emits the TR into the forward hemisphere with an intensity

$$\begin{aligned} \frac{d^2W}{d\omega d\Omega} &= \frac{e^2 v^2 \sin^2 \theta \cos^2 \theta \sqrt{\epsilon_2}}{\pi^2 c^3 (1 - \beta^2 \epsilon_2 \cos^2 \theta)} \\ &\times \left[\left((\epsilon_1 - \epsilon_2) (1 - \beta^2 \epsilon_2 - \beta \sqrt{\epsilon_1 - \epsilon_2 \sin^2 \theta}) \right) \right. \\ &\times \left((1 - \beta \sqrt{\epsilon_1 - \epsilon_2 \sin^2 \theta}) \right) \\ &\left. \times \left(\epsilon_1 \cos \theta + \sqrt{\epsilon_1 \epsilon_2 - \epsilon_2^2 \sin^2 \theta} \right) \right]^{-1} \quad (2) \end{aligned}$$

For the relativistic case, many new features of TR can be obtained. For instance, for the opposite direction of the velocity, i.e., when the particle moves from a medium to vacuum, the sign of β in all terms must be reversed. Thus, in contrast to a nonrelativistic particle, the radiation in the present case depends on the sign of the particle velocity with respect to the medium, i.e., a characteristic directionality appears in this case.

The most attractive feature is that TR by relativistic particles also extends into the X-ray region. For simplicity, let us assume that $\epsilon_1 = \epsilon$ and $\epsilon_2 = 1$ corresponding to the case when the incident particle passes the boundary from medium to vacuum. The energy flux in the vacuum because of transition radiation is found to be

$$\begin{aligned} \frac{dW}{d\theta} &= \frac{2e^2 \beta^2}{\pi c^3} \frac{\sin^2 \theta \cos^2 \theta}{(1 - \beta^2 \cos^2 \theta)} d\omega \\ &\times \left[\frac{(\epsilon - 1)(1 - \beta^2 - \beta \sqrt{\epsilon - \sin^2 \theta})}{(1 - \beta \sqrt{\epsilon - \sin^2 \theta})(\epsilon \cos \theta + \sqrt{\epsilon - \sin^2 \theta})} \right]^2. \quad (3) \end{aligned}$$

For relativistic particles ($\gamma = E/m \gg 1$), it can be seen that the radiation has a sharp maximum at a small angle. The term $(1 - \beta^2 \cos^2 \theta)$ in the denominator becomes minimum at the angle of order $1/\gamma$ because the term can be approximated as

$$1 - \beta^2 \cos^2 \theta = 1 - (1 - \gamma^{-2}) \cos^2 \theta \approx \gamma^{-2} + \theta^2$$

for large γ and small angle ($\gamma = 1/(1 - \beta^2)^{1/2}$). The greatest contribution to the spectrum results when the deviation of ϵ from unity becomes small. The expression for ϵ at high frequency is given by

$$\epsilon = 1 - \omega_p^2 / \omega^2 = 1 - \xi^2, \quad (4)$$

where

$$\omega_p = \sqrt{\frac{4 n e^2}{m}} = 28.8 \sqrt{\rho \frac{Z}{A}} \text{ eV} \quad (5)$$

is the plasma frequency with $\hbar = c = 1$ and n meaning the volume, m the electron mass, ρ the density of material, Z the atomic number, and A the atomic weight. The plasma frequencies and other properties of radiator materials are given in table 1.

The deviation of ξ^2 from unity at high frequencies can approach the same order of $1/\gamma$. Taking this fact into account, the main contribution to expression (3) is at frequencies larger than the optical frequencies because of the small factor in the denominator $1 - \beta(\epsilon - \sin^2 \theta)^{1/2}$. This factor is of the order of γ^{-2} since

$$\begin{aligned} 1 - (1 - \gamma^{-2})^{1/2} (1 - \xi^2 - \sin^2 \theta)^{1/2} \\ \approx 1/2(\gamma^{-2} + \xi^2 + \theta^2) \end{aligned}$$

Table 1
Radiator material properties

Material	Density ρ [g cm ⁻³]	Plasma fre- quency ω_p [eV]	Linear absorption coefficient at 10 keV $\mu\rho^a$ [cm ⁻¹]	Radia- tion length X_0 [cm]
Lithium	0.534	13.8	7.09×10^{-2}	148
Beryllium	1.84	26.1	7.19×10^{-1}	34.7
Aluminium	2.70	32.8	7.14×10^1	8.91
Polyethylene CH ₂	0.925	20.9	1.79×10^0	49
Mylar C ₅ H ₄ O ₂	1.38	24.4	8.07×10^0	28.7
Air	2.2×10^{-3}	0.7	9.1×10^{-2}	30870

^a μ = mass absorption coefficient [cm² g⁻¹].

for $\beta \approx 1$, and $\theta \ll 1$ in the relativistic case. The range of frequencies emitted in the relativistic case will therefore be extended to the X-ray region.

The TR in the first medium (backward radiation) can be obtained in essentially the same way by replacing β with $-\beta$ in eq. (2). The small factor in the denominator disappears and therefore the backward TR is comprised only of the optical part of the spectrum.

2.2. The formation zones

Expressions (2) and (3) describe the transition radiation under the conditions $(\omega/c)R \sin^2 \theta \gg 1$ [6,21,25], where the R is the distance from the point of emergence of the particle from the medium to the point of observation. Within the space region $R \approx (c/\omega) \sin^{-2} \theta$, a redistribution of the TR wave field takes place. As shown in eq. (3), most of the radiation is emitted at an angle $\sin \theta \approx 1/\gamma$ for relativistic particles so that we get $R = \gamma^2 c/\omega$, which is called the "formation zone" in vacuum. In vacuum the formation zone becomes macroscopic in size; e.g., for the particle with $\gamma \approx 5000$ and $\omega \approx 10$ keV, $R \approx 1$ mm.

A formation zone is also obtained in the medium. After Ter-Mikaelyan [23], as a consequence of the interaction with the electron plasma, the longitudinal momentum transferred by the particle to the medium is given by

$$q_{\parallel} = \hbar\omega(1 - \beta\sqrt{\epsilon} \cos \theta). \quad (6)$$

As the incident energy increases ($\beta \rightarrow 1$), q_{\parallel} becomes very small. Therefore, to emit a quantum $\hbar\omega$, it is necessary for the particle to travel a long distance \hbar/q_{\parallel} .

In other words, the phase difference of the photons radiated from two points with a distance z along the path of the particle must be of the order of unity, i.e., $|(\omega/v)z - k z| \approx 1$, which gives

$$z \approx \left| \frac{\omega}{v} - k \right|^{-1}, \quad (7)$$

where v is the velocity of the incident particle and k is the wave number of the radiation in the medium. In the relativistic case its order of magnitude in vacuum is

$$z \approx \frac{2c}{\omega(\gamma^{-2} + \theta^2)}$$

(which reduces to $R \approx \gamma^2 c/\omega$ for the angle $\theta \approx 1/\gamma$) and in the medium at frequencies larger than optical

$$z \approx \frac{2c}{\omega(\gamma^{-2} + \theta^2 + \xi^2)}.$$

An appreciable intensity is obtainable only when a charged particle can traverse a distance of the order of the formation zone in a medium. In fig. 1 formation zones of polyethylene and air are shown as functions of ω for different values of γ . The formation zone of air is roughly 100 times larger than that of polyethylene.

In practice the thickness of the foil is usually 10–20 μm ; this means that the hard part of the TR spectrum is suppressed because of the energy dependence of the TR formation zone in the radiator material.

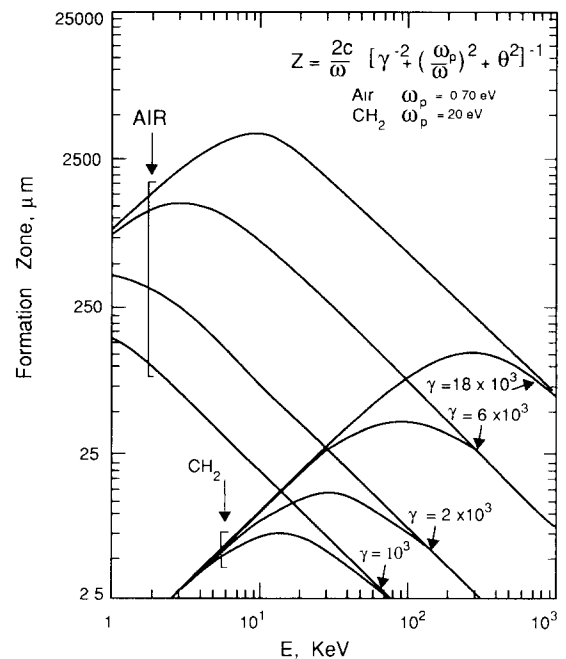


Fig. 1. The formation zones of TR.

2.3. The angular distribution

Substituting eq. (14) into eq. (3) and making approximations for small angles, the intensity reduces to a simple form:

$$\frac{dW}{d\omega d\theta} = \frac{2\alpha}{\pi} f_0(\theta) \tag{8}$$

with

$$f_0(\theta) = \theta^3 \left(\frac{1}{\gamma^{-2} + \theta^2 + \xi_g^2} - \frac{1}{\gamma^{-2} + \theta^2 + \xi_f^2} \right)^2, \tag{9}$$

where α is the fine structure constant (1/137), ω is the energy of the radiated photon, ω_i is the plasma frequency of medium and vacuum, and $\xi_i = \omega_i/\omega$; the indexes g and f mean gas and foil.

In almost all applications the lower density medium is a gas rather than vacuum, and the ω_g term appears as above. The denser medium is usually foil, and will be indicated with suffix f. Fig. 2 shows the angular distribution of the single surface yield (9) for 3 GeV ($\gamma = 6000$) electron energy and radiated energies between 5 and 20 keV. The distribution has a peak at the narrow angle $\theta \approx \gamma^{-1}$ and extends to the angle of order $(\gamma^{-2} + \xi_f^2)^{1/2}$. Because the TR angle $\theta \approx \gamma^{-1}$ is very small, the practical application of the angle measurements is very difficult (see section 3.3).

2.4. TR yield

The integration of expression (8) over the angles θ yields the energy spectrum

$$\frac{dW}{d\omega} = \frac{\alpha}{\pi} \left[\frac{\epsilon_f^2 + \epsilon_g^2 + 2\gamma^{-2}}{\xi_f^2 - \xi_g^2} \ln \frac{\gamma^{-2} + \epsilon_f^2}{\gamma^{-2} + \epsilon_g^2} - 2 \right]. \tag{10}$$

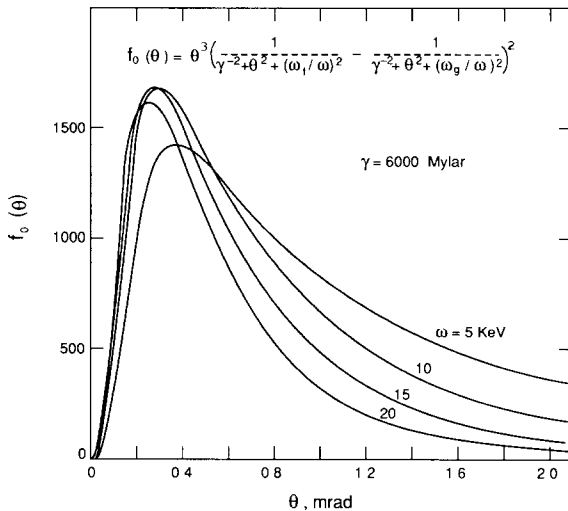


Fig. 2. Angular distribution of a single surface yield.

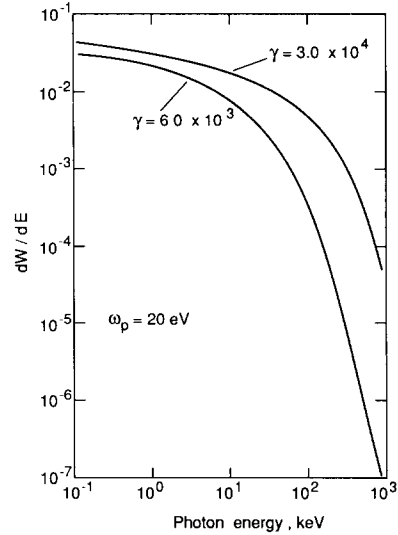


Fig. 3. The radiated TR spectrum from a polyethylene surface.

It follows from eq. (10) for large ξ_f^2/ξ_g^2 (usually of the order of 10^3) that there exists a cutoff frequency $\omega_c = \omega_f \gamma$ such that

$$\begin{aligned} \frac{dW}{d\omega} &= \frac{e^2}{6\pi c} \left(\frac{\omega_c}{\omega} \right)^4 \quad \text{for } \gamma \ll \xi_f^{-1}, \text{ i.e., } \omega \gg \omega_c, \\ \frac{dW}{d\omega} &= \frac{2e^2}{\pi c} \ln \frac{\omega_c}{\omega} \quad \text{for } \xi_f^{-1} \ll \gamma \ll \xi_g^{-1}, \text{ i.e., } \omega \ll \omega_c, \end{aligned} \tag{11}$$

and

$$\frac{dW}{d\omega} = \frac{2e^2}{\pi c} \left(\ln \frac{\omega_f}{\omega_g} - 1 \right) \quad \text{for } \gamma \gg \xi_g^{-1}.$$

The spectrum from a single surface is a monotonically decreasing function of radiation energy and it drops as rapidly as ω^{-4} at high frequencies. Fig. 3 shows a spectrum from a surface of polyethylene for $\gamma = 6000$ and 30000. The high photon-energy component becomes stronger when γ increases.

A very important result of TR from relativistic particles is obtained by the integration of spectrum (10) ($\xi_g = 0$):

$$W_{TR} = \frac{1}{3} \alpha \omega_f \gamma = 2.43 \times 10^{-3} \omega_f \gamma. \tag{12}$$

The main contribution in the integral is due to frequencies which are not too small compared with the limiting frequency. More than 95% of the energy is produced in the range of $0.1 \omega_c < \omega < \omega_c$ (e.g., for $\omega_f = 0.02$ keV and $\gamma = 5000$, we obtain $10 \text{ keV} < \omega < 100 \text{ keV}$). It should be noted, that measurements with detectors which are only sensitive in a limited fre-

quency interval would, in general, not follow a linear γ -dependence.

Finally we consider the number transition radiation photons. The number of photons with frequencies greater than a lower limit ω is given by the expression

$$N(>\omega) = \frac{\alpha}{\pi} \left\{ \ln \frac{\omega_c}{\omega} \left(\ln \frac{\omega_c}{\omega} - 2 \right) + \frac{\pi^2}{12} + 1 \right\}. \quad (13)$$

For instance, for $\omega_c = 100$ keV, $\omega = 1$ keV we obtain $N(>1 \text{ keV}) = 0.03$ foil⁻¹. The statistics of TR photons is described by a Poisson distribution [24]. Because of the small probability for an energetic photon emission per particle transition through one interface ($N \approx \alpha$), we need a large number of interfaces for practical applications. To achieve this, a stack of many foils with gaps in between is used in practice.

Let us estimate the TR yield produced by a particle passing through a dielectric foil with thickness t placed in vacuum. The field at the observation point is given as a sum of fields produced at both surfaces of the foil. For relativistic particles, the amplitudes of the forward radiation from both surfaces have the same magnitudes. Hence, we consider only the phase difference between the fields. The phase change of the field produced at the first surface is $kt \cos \theta$ when it reaches the second surface, where k is the wave number of the emitted TR. The generation of the field from the second surface occurs later in time with the corresponding phase lag $\omega t/v$ relative to the first field; this field also has a phase difference π compared to the field from the front surface due to the opposite sign of its polarization. By summing the two fields, we obtain an interference factor for amplitudes:

$$|e^{ikt \cos \theta} - e^{i\omega t/v}|^2 = 4 \sin^2((kt \cos \theta - \omega t/v)/2). \quad (14)$$

The yield from one layer of medium in a gas is therefore given by

$$\frac{d^2 W_{\text{SF}}}{d\omega d\theta} = \frac{2\alpha}{\pi} f_0(\theta) f_1(\theta), \quad (15)$$

where

$$f_1(\theta) = 4 \sin^2(\phi_f/2), \quad (16)$$

with

$$\phi_f = kt \cos \theta - \omega t/v.$$

By using the relations $k = \omega/c \sqrt{\epsilon}$ and (4) and approximating $\cos \theta \approx 1 - \theta^2/2$ and $\beta^{-1} = 1/(2\gamma^2)$, we obtain

$$\phi_f = (\omega t_f/2c)(\gamma^{-2} + \theta^2 + \xi_f^2). \quad (17)$$

If the foil thickness t_f is much smaller than the "formation zone" of the foil,

$$z_f = (2c/\omega)(\gamma^{-2} + \theta^2 + \xi_f^2)^{-1},$$

the yield is strongly suppressed by the interference factor. If the foil thickness is much greater than the formation zone of the medium, then the interference term has the value of 2 and the foil radiation becomes twice of that for one boundary.

Similarly, the amplitude for N foils equally spaced in gas is just the sum of N amplitudes each advanced by phase ϕ

$$a_N = a_1(1 + e^{i\phi} + e^{2i\phi} + \dots + e^{(N-1)i\phi}), \quad (18)$$

where a_1 is the single foil amplitude and

$$\phi(k_f \cos \theta - \omega/v)t_f + (k_g \cos \theta - \omega/v)t_g,$$

with wave numbers $k_i = (\omega/c)\sqrt{\epsilon_i}$ in each medium. By completing the summation, we find the intensity ratio of N foils to a single one to be

$$f_N(\theta) = |a_N|^2/|a_1|^2 = \sin^2(N\phi/2)/\sin^2(\phi/2). \quad (19)$$

As the formation zone of air is about 100 times larger than that of the dielectric medium, an appreciable yield from the N -foil stack will be obtained only if the foils are spaced by the order of the air formation zone (see fig. 1).

If the spacing between foils is larger than the air formation zone, we obtain the numerical values of the energy spectra by using the single foil formula approximation. This means, that the total flux (or number of TR photons) emerging from a foil stack is approximated as an incoherent sum of radiations from N foils.

The expression for the total flux then represents the integration with respect to the emission angle θ and a factor which describes the incoherent addition of the single foil intensities which includes also the absorption of TR photons in the radiator materials (foils and gas).

This absorption is expressed as

$$N_{\text{eff}} = \frac{1 - e^{-N\sigma}}{1 - e^{-\sigma}}, \quad (20)$$

where $\sigma = (\mu\rho t)_f + (\mu\rho t)_g$ with μ , ρ and t meaning the absorption coefficient, the density, and the thickness of the material respectively. So the total flux from a foil stack is therefore given by

$$\frac{dW}{d\omega} = \frac{2\alpha}{\pi} N_{\text{eff}} \int_{\text{with absorption}} f_0(\theta) f_1(\theta) d\theta. \quad (21)$$

The angular limits of the integral depend on the frequency of the emitted radiation, which in turn is governed by the absorption within the foil materials.

The absorption of TR in the foil materials prevents an infinite amount of radiation yield from a foil stack. In fact, there exists a certain limit for the number of foils, and the yield (fig. 15) saturates at $N_{\text{eff}} \Rightarrow (1 - e^{-\sigma})^{-1}$ for $N \Rightarrow \infty$.



Fig. 4. The first detection of TR X-rays in a streamer chamber [30].

For most practical cases, when the distance between the foils is of the order of or less than the air formation zone, the amplitude for N foils is the coherent sum of N amplitudes (18). The total flux (or number of TR photons) from a foil stack must be obtained by numerical integration including the absorption losses or by applying special analytical approximations [25].

In reality the design of transition radiators is dominated by the consideration of interference effects. This becomes obvious if we consider the strongly decreased TR emission when the foil thickness approaches zero, or when the gaps between the foils vanish. These effects are usually expressed in a different way, i.e. by saying that the transient field exists over a certain region, which is the formation zone. However, the interference effects are still important even if the foil thicknesses and gaps are larger than the corresponding formation zone (at a level of 20–30%).

The most important consequence of the interference effects is the saturation of the X-ray yield above a certain γ -value. For this case the yield drastically deviates from what we expected for an incoherent addition of single foil yields, and it shatters our dream to determine γ for very high energy particles via the

observed number of X-ray photons. However, it should be remarked that the particle energy at which the saturation sets in can be varied by changing the radiator parameters (foil thickness, gap, etc.).

The theoretical expression for the TR X-ray yield in the multifoil case is quite complicated and not transparent, and a numerical computation is necessary to predict exactly how a detector will work (such a Monte Carlo program was developed in ref. [26], for instance). However, several efforts were done to use “practical” TR theory [25,27,28]. Ref. [25] has been in particular successful for first approximations; these authors introduce three dimensionless variables and use a universal function for the spectral distribution. Approximate relations expressed in these small number of dimensionless variables are useful in designing detectors. Such an application is found in ref. [19].

3. Methods of TR detection and experimental evidence of the main features of TR

3.1. First observations of TR

Here we will describe two most interesting examples of TR observations carried out by Armenian physicists during the sixties. The first observation of TR [29] was done with high energy cosmic muons. The high energy particles passed through many paper sheets; the X-ray TR photons were absorbed in Kr gas. The characteristic fluorescence photons emitted from the K-line of krypton were detected with a NaI crystal. The rate of detected fluorescence photons was found to be in good

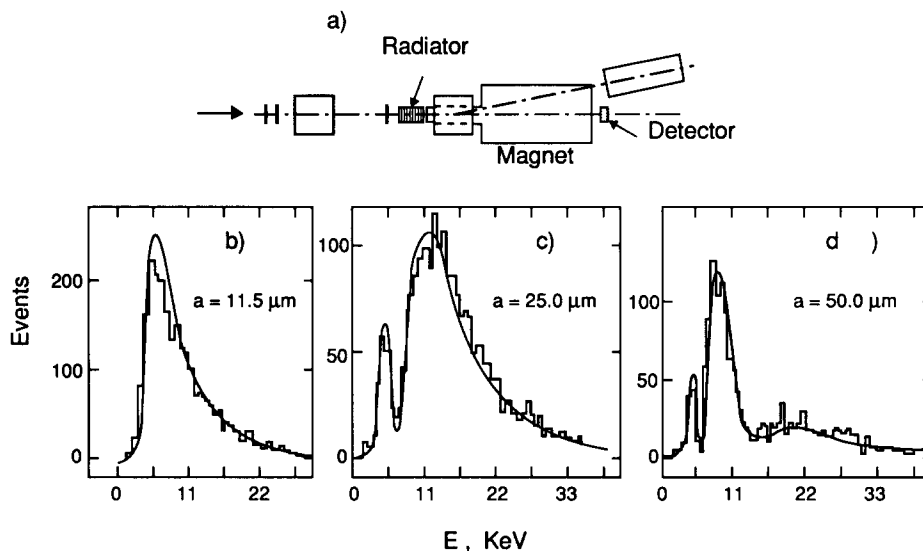


Fig. 5. TR X-ray frequency spectra (b) measured with a solid state detector in a setup shown above (a). The curves are predictions of the theory for different foil thicknesses.

agreement with the expected rate. Of course, the efficiency of TR photon detection was very low because of the small solid angle covered by the NaI detector, and only a small part of the TR spectrum contributes to the fluorescence excitation above the K-edge of krypton ($E_K = 14.3$ keV).

Another nice example is TR photon detection is by using a streamer chamber [30]. In this example the TR radiator was located a few meters upstream the streamer chamber in an electron beam with energies between 1.2 and 2.46 GeV. In order to increase the detection efficiency for TR photons (photon energy: 5–15 keV), 70% of xenon was added to the neon gas of the streamer chamber. Owing to the TR emission angle ($\approx 10^{-3}$ relative to the electron track), the absorption of X-rays in the streamer chamber gas took place at a few millimeters distance from the electron track (see fig. 4). A very impressive picture of TR has been obtained in this way.

3.2. The magnetic separation of the TR photons and particle tracks

A gaseous detector placed behind a radiator responds to both the TR X-rays and the particle ionization. However, a magnetic field can be used to separate the TR photons from ionization produced in the photon detector by the charge track [31].

The magnetic separation between particle tracks and TR photons is very useful to perform more convincing tests of the TR theory. For instance, the authors of ref. [32] measured energies of individual TR photons emitted in TR radiator in front of a magnet by a solid state detector, located just behind the magnet, which separated X-rays and particle tracks (fig. 5a). The TR radiator consists of a small number of foils in order to yield an average number of less than one

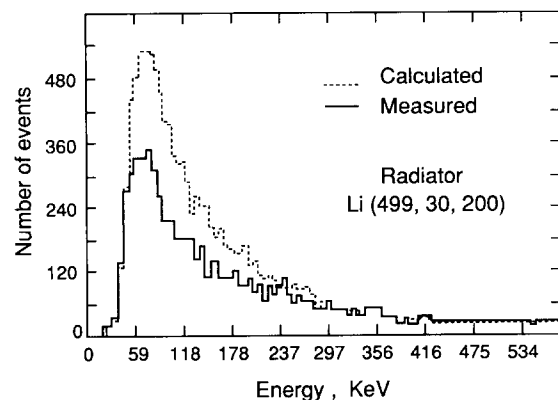


Fig. 6. Comparison of measured TR yield for Li foils radiator with theory predictions.

emitted photon per particle. Thus the confusion due to multiple photon emission by each particle has been avoided, and the frequency spectra have been obtained for different thicknesses of foils (fig. 5). The event rates peak at certain “oscillating” photon energies depending on the foil thickness, in agreement with the predictions of coherent TR emission as shown in fig. 5. Similar results were obtained by means of an X-ray diffraction on a crystal [33,34].

The same method of magnetic separation of TR X-rays and particle tracks was applied [19] to measure the TR spectrum of 499 Li foils within the radiator (50 μm foil thickness with 200 μm spacing (fig. 6)). Measured and calculated spectra have similar shapes, but the TR yield for the Li foils is 30–40% lower than predicted by TR theory. Other types of radiators (Mylar, CH_2) gave better agreement in the total yield with TR theory (10–15%). The disagreement in case of Li foils is pointed out by several authors [35] and is still unexplained today.

Finally we note, that the magnetic separation method has a limited application, because the magnet requires space which is often not available, except for particle identification just on the beam line.

3.3. The use of the angular separation between TR photons and particle track

TR theory predicts an angular photon emission (relation (8)) for single surface yield (see also fig. 2) with typical peaks at an angle $\theta \approx 1/\gamma$ and extends to an angle of the order of $(\gamma^{-2} + \xi_f^2)^{1/2}$. The theory with complete coherence for a multifoil radiator [22] gives an angular distribution which should exhibit many sharp cones, depending on the photon energy.

Detailed measurements of these energy–angle distributions seem impractical due to overlap effects arising from Compton scattering of TR photons, finite energy resolution of the photon detector and multiple scattering of the particle in the radiator. Since the photon detector integrates usually over some energy interval (5–20 keV), it yields, because of multifoil radiator interference effects, an average TR intensity, which is about half of that shown in fig. 2 [36].

It is difficult to apply the angular characteristics of transition radiation, because the emission angle is very small ($\approx 1/\gamma$), and the spatial separation between the particle track and TR emission is therefore in general very difficult. For electrons, however, the ratio of the multiple scattering angle in the radiator materials and the TR angle becomes large:

$$\frac{\theta_{\text{m scatt}}}{\theta_{\text{TR}}} = \frac{21 \text{ MeV} \sqrt{x/x_0}}{p\beta} \frac{E}{mc^2} 40 \sqrt{\frac{x}{x_0}} = 10 \quad (22)$$

for $x/x_0 \approx 0.05$.

According to this relation, the angular distribution due to multiple scattering of electrons in the radiator foils is one order of magnitude larger than the emission angle for TR photons.

Qualitatively spatial separation between charged tracks and TR photons has been performed in a streamer chamber [30] (fig. 4). More quantitatively the use of additional information from track-photon separation has been demonstrated elsewhere [37,38]. In ref. [36] a scintillation drift chamber with very high space resolution ($\approx 20 \mu\text{m}$ in xenon at a pressure of 10 bar) was used as a TR detector. The simultaneous use of spatial and energy information is shown in fig. 7, which presents a two-dimensional distribution of events without TR (pions, fig. 7a) and with TR (electrons, fig. 7b). It is obtained from two of the above mentioned drift chambers mounted about half a meter behind radiator foils. The first chamber detects TR photons and dE/dx of the particles. The second one, separated from the first by a photon absorber, detects dE/dx signals only and gives the position of the particle track. The vertical axis in fig. 7 shows the energy deposition, and the abscissa denotes the difference between the center-of-gravity of the charge for two chambers. The difference between pions and electrons ($E = 3.5 \text{ GeV}$) is evident. However, this method is not applicable for the construction of large aperture detectors because of the high pressure (10 bar) needed to achieve the necessary high space precision.

Another attempt to use the angular separation between the charged track and the TR photon was made in ref. [38], where a drift chamber at normal pressure and Li-foils radiators were used for π/K separation

was demonstrated. Because of the relatively poor space resolution of the drift chamber, the distance required between the TR radiator and the detector had to be larger than 1 m. This results in a considerable increase of the total TR detector length and consequently limits its application.

3.4. Conventional TR detectors: multiset xenon filled proportional chambers (PC)

Since the seventies it has been established as a common technique to detect both X-rays and dE/dx losses by a proportional chamber behind a TR radiator (stack of regularly spaced foils or plastic foam). In such an apparatus, one obtains the average X-ray energy deposited to the gas per incident particle, by subtracting the average dE/dx of the particle from the observed signal. An example for this method [18] is shown in fig. 8. The resulting yield is obtained by integrating over the energies and the angles of all TR photons. A test of the TR theory would be to measure this yield as a function of different free parameters:

- foil thickness [27] (fig. 9);
- number of foils [27] (fig. 10);
- X-ray yield [19] (fig. 11) as a function of γ ; and
- number of TR photons [39] (fig. 12) as a function of γ .

In these figures, the curves result from calculations which took into account the full coherence effects, X-ray absorption in the foils, and X-ray detection efficiency. Although a discrepancy in absolute yield for the Li-foil radiator (as mentioned above) exists, the

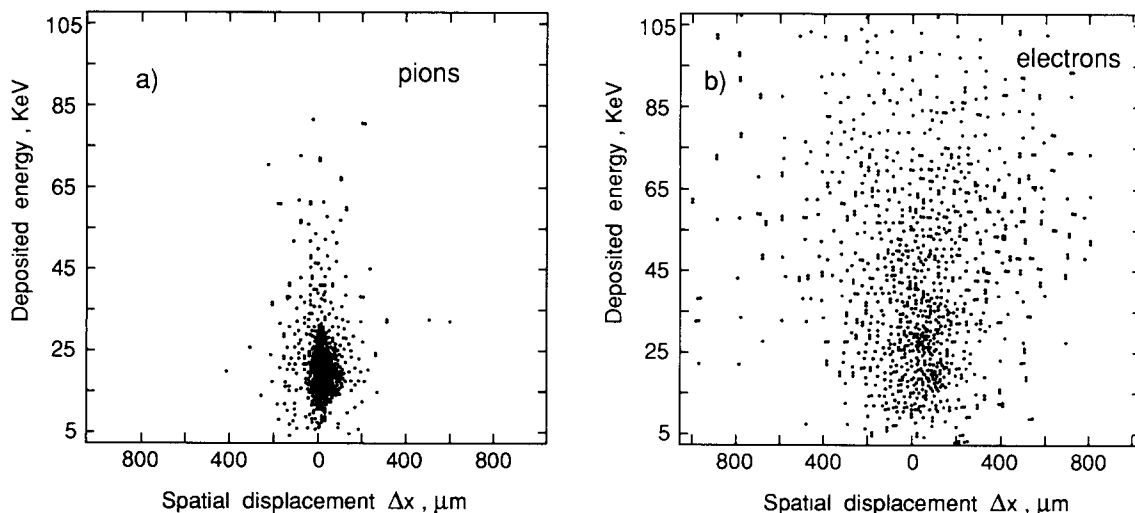


Fig. 7. Two-dimensional distributions of the events: energy deposition E in the detector vs spatial displacement of the center of gravity of the charge Δx for pions (a) and electrons (b). Smearing is enhanced in the case of electrons (b) due to the detection of TR photons.

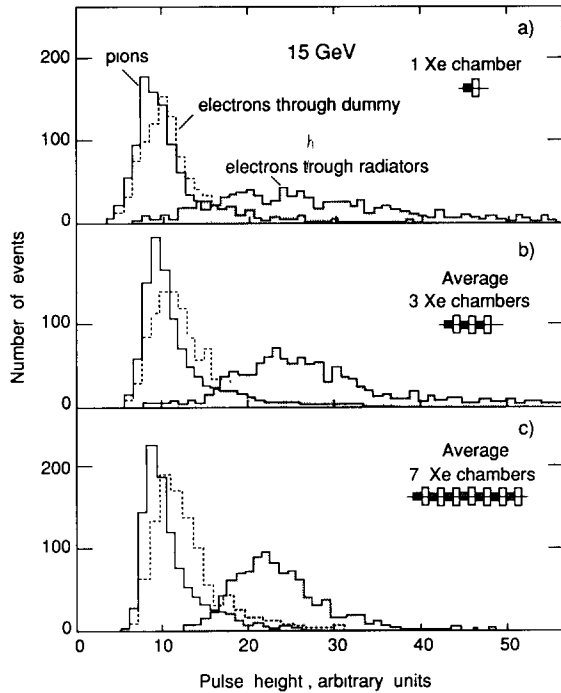


Fig. 8. Averaged pulse height spectra for 15 GeV/c pions and electrons observed in various number of TR sets.

dependences of all parameters are correctly predicted by the calculation. At low Lorentz factors γ , in the 100 GeV range for hadrons, the X-ray are emitted with lower energies and therefore thinner foils should be adequate, according to the reduced formation zone (see fig. 1). The results of such an attempt are shown in fig. 13 [40]. X-rays emitted from 4000 thin (3–10 μm) Mylar sheets are detected by Chambers, filled with different xenon proportions.

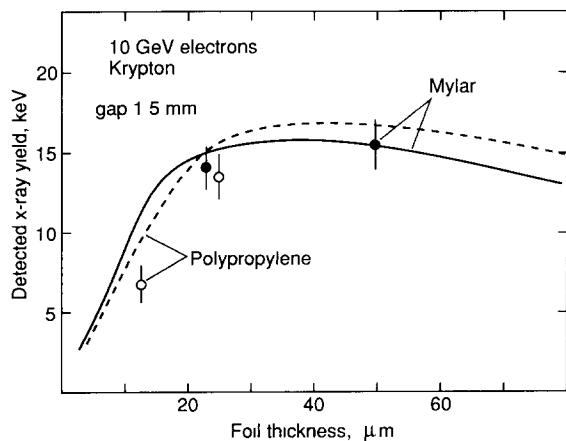


Fig. 9. Comparison of the observed X-ray yield (measuring points) with theory curves for different foil thicknesses.

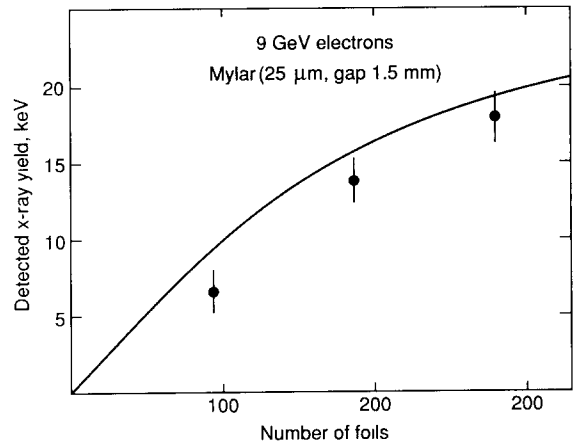


Fig. 10. Comparison of the observed X-ray yields (measuring points) with theory curve for a various number of foils.

TR is emitted at any sharp boundary of macroscopically thick materials, and thus the regular spacing of boundaries is not very essential. Instead of a foil stack, we can imagine various types of radiators: liquids or solids containing many gas bubbles, powders, fibers, small particles suspended in liquids, etc. TR X-rays have in fact been detected when high energy charged particles passed through plastic foam [41–43]. The yield can be calculated by using the average and the variance of the bubble sizes and the air spacings. The calculation reproduces the observed X-ray yield (fig. 14) [42].

4. Design of an optimum TRD

It is important to optimize the many parameters in the overall TR system. This is particularly important

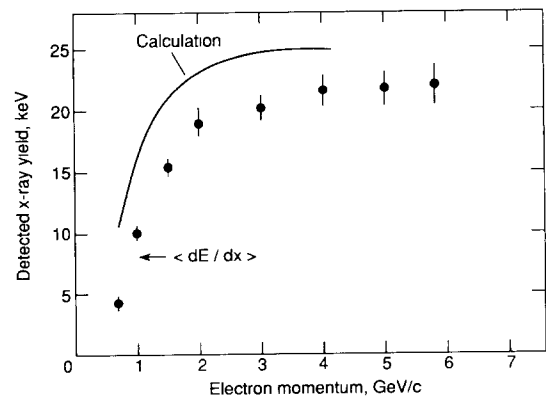


Fig. 11. Comparison of the observed X-ray yields (measuring points) with theory for various electron momenta (TR radiator: Li foils).

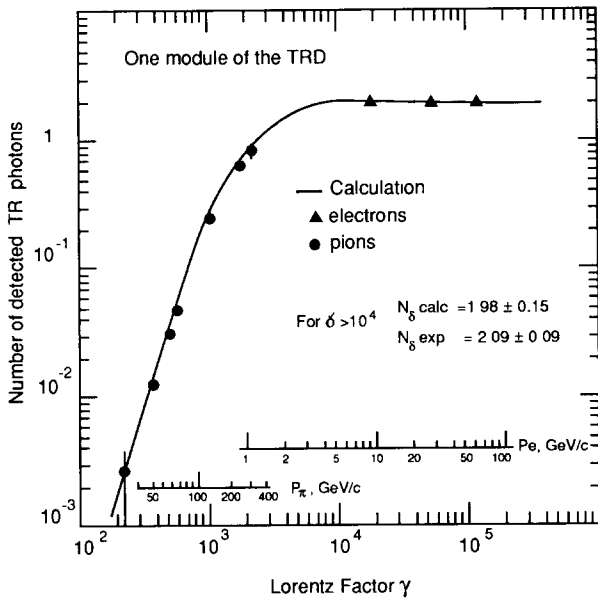


Fig. 12. Comparison of the detected number of TR photons with MC calculation for various γ -values (TR radiator: CH_2 foils).

because of the small number of produced TR photons. Therefore, this section considers:

- the material and structure of TR radiators (regular or randomly spaced, thickness of foils and gaps, the number of foils etc.);

- the characteristics of TR proportional (drift) chambers (gas composition and its properties: thickness, drift and diffusion of electrons, etc.);
- the number of radiator-detector sets for a given total length of the TRD (“granularity” of the TRD); and
- the total thickness of the TRD (in radiation or interaction lengths).

The crucial aspect for optimization is the identification capability of the TRD, expressed by its rejection factor R . Its value is defined for two kinds of particles (1 and 2) with different Lorentz factors $\gamma = E/mc^2$ as:

$$R_{1/2} = \eta_1/\eta_2 \quad (23)$$

(usually $\eta_2 = 90\%$), where η_1 and η_2 mean the detection efficiencies of particles 1 and 2, respectively.

4.1. Two methods of TRD signal processing

The essential aspect of TRD operation is signal processing. So far two methods of signal processing have been mainly used:

- 1) total energy deposition (“Q-method”); and
- 2) cluster counting [44,45] (“N-method”)

In the first method (mentioned in section 3), the signals are amplified by a charge sensitive amplifier and pulse-analyzed by ADCs. In this way the energy deposited by the ionizing particle and by the transition radiation photons is measured. Since the energy released by a radiating particle (large γ) is on average larger than that from a nonradiating particle, the discrimination is based on an energy cut. The main factor

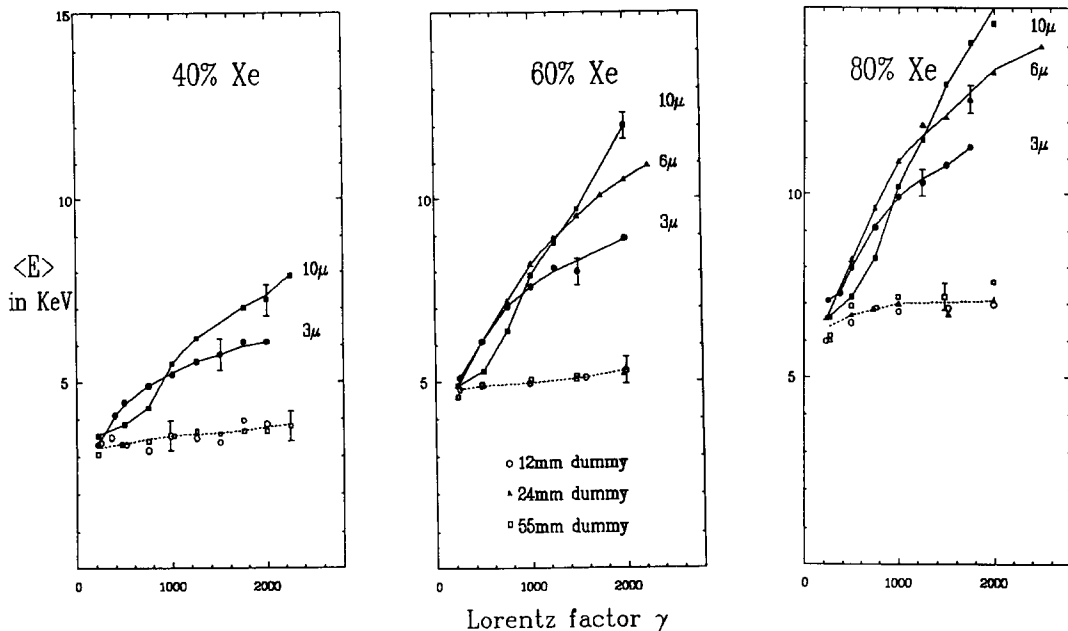


Fig. 13. γ -dependence of the energy loss in a xenon chamber for a radiator of 4000 Mylar foils (thicknesses range from $3 \mu\text{m}$ to $10 \mu\text{m}$).

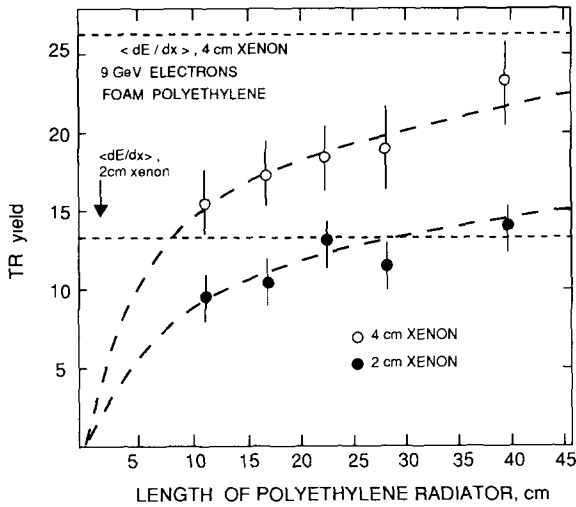


Fig. 14. Comparison of the observed (measuring points) and the calculated (curves) yields for plastic foam radiators.

limiting the rejection of nonradiating particles (small γ) in this case is the Landau “tail” of ionization loss, which simulates a large energy deposition comparable with that of a radiating particle.

With the second method the avalanches produced by X-ray photoelectrons are recorded and counted when they exceed a given threshold (typically 4–5 keV). The counting of these avalanches, which are due to the ionization clusters from electrons of some keV, gives the possibility to select high γ particles. Non-radiating particles should provide fewer detectable clusters due to occasional δ -rays produced in the same X-ray energy range [44,45]; the distribution of these δ -rays is Poissonian.

There are important distinctions between the above two methods (Q and N) of signal processing:

- The optimization of the TRD system is slightly different. The detection of high energy TR photons is more important for the Q-method because of their large contribution to the total energy deposition. For the N-method, the number of relatively soft TR photons determines the Poisson statistics (compared to the Q-method thinner foils and detector gas layers are needed);
- The readout for the two methods is also different. ADCs (or FADCs) are needed for the Q-method. Fast triggering is difficult in this case. The cluster counting (N-method) requires fast discriminators and scalers and is very favourable for fast ($< 1 \mu\text{s}$) triggering.

In general, the cluster counting (N) method, should be the best method due to the distinction of the Poisson distributed number of the ionization clusters produced by nonradiated particles against the Landau tail of dE/dx losses in case of Q-method. But the

comparison of the two methods is complicated and should be done for each individual case [44–46], because of the different optimum structures required for both methods and the problem of the cluster counting ability of TR chambers (see below).

Our consideration will be related mostly to the cluster counting method (N), bearing in mind that the optimization of TR radiators and chambers for both methods is slightly different.

4.2. Choice and optimization of TR radiator

A statistical meaningful detection of TR X-photons is only possible by using a multilayer stack of radiator foils. As mentioned above, the use of less absorbent radiator materials allows an increase in the number of foils in order to improve the TR yield. To describe a radiator stack we use the notation (N, t_f, t_g) , where N is the number of foils, t_f is the foil thickness (μm), and t_g is the gap thickness (μm), respectively. The name of the radiator material will be placed before the parenthesis.

The typical average energy of TR photons is 7–10 keV for practical radiators. The TR spectrum becomes softer if we use foil materials with smaller plasma frequency and/or thinner foils.

The yield from a foil stack increases with the foil number N up to the saturation limit, which marks the equilibrium between emitted and reabsorbed X-ray photons. The effective number of foils N_{eff} at a certain energy is given by relation (20). When the number of foils N becomes large, N_{eff} approaches the value $(1 - e^{-\sigma})^{-1}$, i.e. the TR yield is saturated. The effective number of foils N_{eff} varies depending on the photon energy (fig. 15), since the X-ray absorption coefficient μ decreases ($\sigma = (\mu\rho t)_f + (\mu\rho t)_g$).

In table 1 the plasma frequency ω_p and the absorption coefficient of some materials are listed. The dependence of the X-ray absorption on the energy and the Z of some absorbers is shown in fig. 16.

For the energy range in question the absorption is dominated by the photoelectric effect. The absorption increases as Z^4/ω^3 , while the TR total energy is roughly proportional to the plasma frequency ω_p of the material, which varies as $Z^{1/2}$. Therefore, if we want to increase the number of photons from the stack, it is preferable to use foils of small Z as radiator material.

Once the particle momentum and therefore its Lorentz factor γ has been decided upon as a working range of the TR detector (for a given ω_p) the foil thickness t_f must be kept as close as possible to its formation zone limits. In this way the largest yield from the same weight of radiator material will be obtained, since we can use more foils for the same self-absorption. The spectrum must, however, remain hard enough to pass through the window of the X-ray detector.

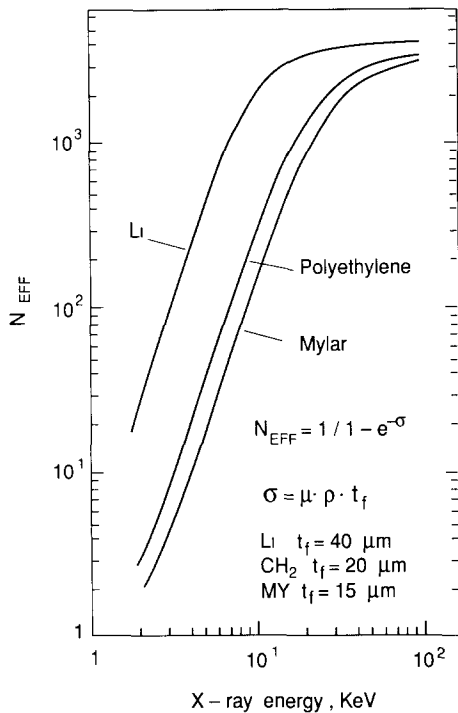


Fig. 15. The effective number of the foils in a TR radiator for different X-ray energies.

If we avoid cryogenic materials, i.e., hydrogen and helium [47], the available solids with very low Z are lithium, lithium hydride and beryllium. Lithium hydride looks attractive since it has an effective Z lower than the pure metal and a substantially higher density. It could conceivably be cast or pressed into thin sheets, but with lithium it is hazardous, in particular if it is divided in thin foils. Beryllium also has a favorable high density, but it is quite expensive in the form of thin foils, and its handling is difficult because of its toxic character. Beryllium scales are more available and cheaper, but the optimization of a practical radiator made of beryllium scales is very difficult: the great spread in scale sizes and the relatively small average gap in between the scales diminish the advantages of such a radiator (see below, fig. 17).

It has been found [19], that it is possible to make satisfactory radiators from pure lithium. It can be rolled to thin sheets (30–40 μm) and formed in such a way that it becomes self-supporting. However, its inflammability and its tendency to react strongly with water (hot flame but without explosion) ask for a thin layer of oil on the foil surfaces, in order to diminish their reactivity. This oil layer gives rise to a 25% excess X-ray absorption.

Even taking into account its softer X-ray spectrum, the lithium radiator has twice the effective number N_{eff}

of foils (see fig. 15) than the polyethylene radiator. This means that the predicted TR yield in the case of Li foils should be ≈ 1.5 times higher, if we also consider its plasma frequency (see relation (9)). In practice, as was mentioned above (see fig. 6 [19]), the TR yield generated by Li foil radiators is less intensive in the soft part of the spectrum than expected. The comparison between lithium and CH_2 radiator [34] is shown in fig. 17. Each point on this figure corresponds to a certain detection energy threshold for ionization clusters formed in the Xe-gas of the drift chamber by TR photon absorption and/or dE/dx ionization losses. Higher ordinate values of the curve mean a better pion/electron rejection. Comparison with the theoretical prediction (solid curves) gives a good agreement in the case of the CH_2 radiator, but we find again a 30–40% difference for the Li-radiator. From fig. 17 we can conclude that Li and CH_2 are about equally suited as TR radiators. On the other hand, Li foils are much less practical because of their chemical reactivity. Fig. 17 also shows the result for a powder radiator made of beryllium scales. As mentioned above, the average packing density of such a radiator cannot be made low enough, which results in a relatively low TR yield.

Different structures of stacked polypropylene fibers [35,48–50] with packing densities between ≈ 0.1 and 0.15 g/cm^3 and also carbon fibers [44] have been

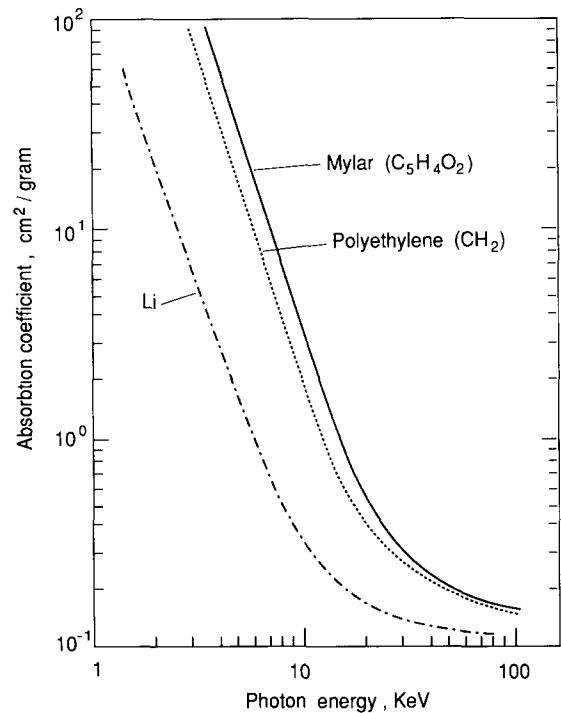


Fig. 16. Absorption coefficients μ of Mylar, polyethylene and lithium.

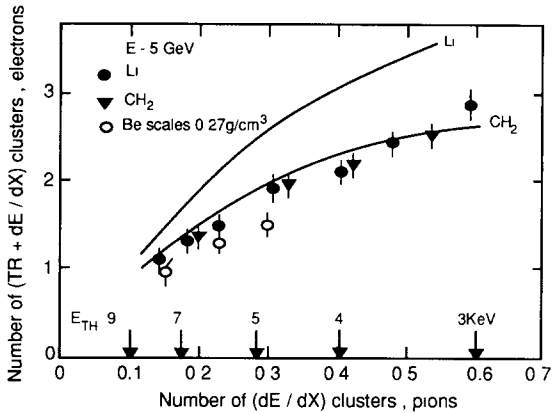


Fig. 17. Comparison of measured TR yields (points) from different radiators; the solid curves are TR theory predictions. E_{th} means the detection energy threshold for ionization clusters.

tested as TR radiators. However their TR yield was only $\approx 80\%$ as compared to CH_2 foil radiators.

In the case of a “compact” TRD (total length < 1 m, essentially for collider experiments) the particle identification power of a TRD depends very strongly on the TR radiation ability:

$$A_{TR} = dN_{\text{photons detected}}/dL_{TRD}. \quad (24)$$

For example, a 15% change of radiation ability gives a factor of about 2 in rejection power. The best achievable value for a compact TRD is $A_{TR} \approx 0.2$ [35] (taking into account the total thickness of the detector); this corresponds to about 200–300 μm gaps between the CH_2 foils. Fig. 18 shows for different gaps the A_{TR} for a TRD radiator made of CH_2 (polypropylene) as a function of foils thickness. This MC simulations were done for a fixed total length for a TRD set of 90 mm. The optimum number of foils is about 300 μm according to the absorption properties of polypropylene (see fig. 15) for the TR spectrum of this case (fig. 19). The optimization of the foil thickness is also shown in fig. 18 and demonstrates the broad optimum around the value of 20 μm .

Around 20 μm foil thickness the γ -dependence of the TR yield is not sensitive to the foil thickness, but depends on their gap values (fig. 20). However, in order to extend the energy region for particle identification considerably, we need to increase the gap value as E^2 (see section 2.2.), which lengthens the TRD quadratically with the particle energy E .

In fixed target experiments the radiators for TRDs can be made out of thin CH_2 foils, which are supported by special frames [35,39]. However, due to stringent limits on mass and dimensions for these devices in collider experiments, such traditional radiators are less satisfactory, since they are not self-supporting.

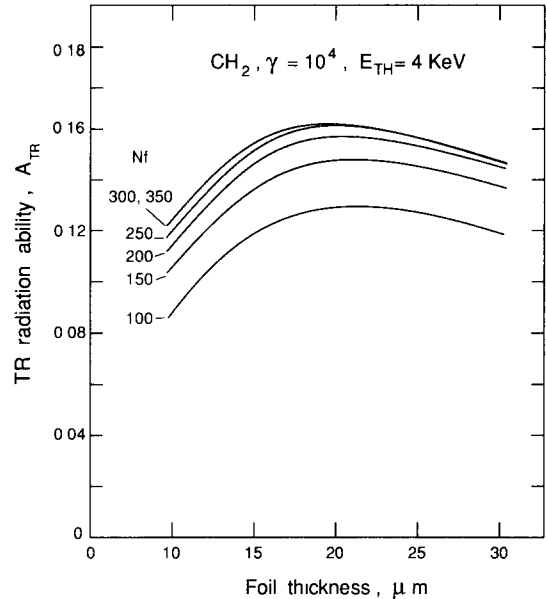


Fig. 18. The MC optimization of one $\text{CH}_2 + \text{Xe}$ TRD set (sized length 90 mm, xenon thickness is 15 mm). The TR radiation ability is optimized as a function of the foil thickness and a the number of foils.

In the $D\phi$ experiment the polypropylene foil has been wound to form a roll which served as a radiator [51]. Here is still some disadvantage because the important parameters (uniform foil and gap thickness) of the radiator vary with the polar angle of the particle trajectory. Besides, a radiator of that kind cannot serve as a supporting structure for the TR detector.

It is important to design a self-supporting radiator with isotropic structure which could also possibly be used as a construction element. Foam materials look

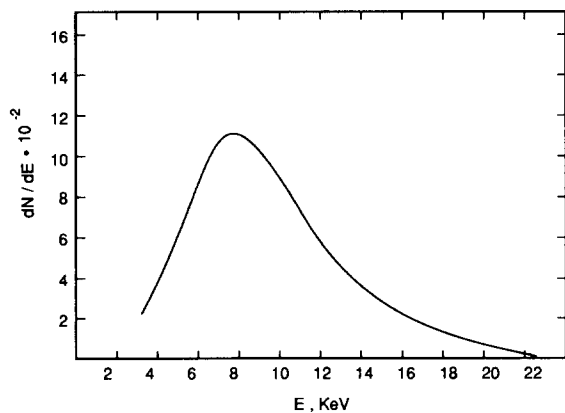


Fig. 19. The spectrum (MC calculation) of absorbed TR X-rays for optimized CH_2 -radiator (fig. 18); the total length of the TRD set is 90 mm, the thickness of Xe gas is 15 mm.

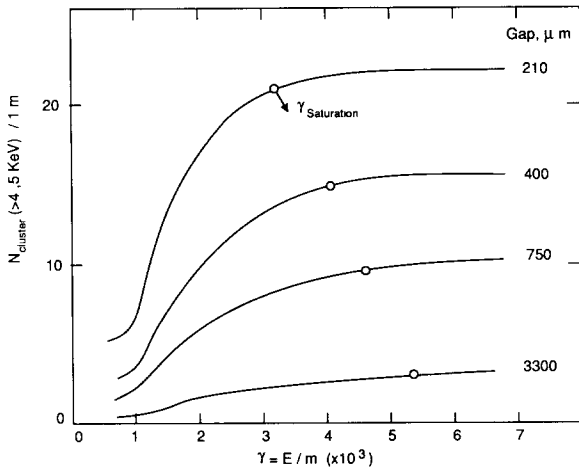


Fig. 20. γ -dependence of the number of TR photons for 1 m total TRD length, foil thickness of 20 μm and gaps as indicated. Each TR (CH_2 foils + Xe) module consists of 300 radiator foils and 15 mm Xe layer for TR detection.

very promising for this purpose and there exists a great variety of foams that could be potentially useful for application in TRDs [53].

Some results from studies on foam radiators can be found in ref. [54,55]. Unfortunately, these results are not comprehensive because the transition radiation yield was measured for a limited range of radiator densities and for thick radiators only. One also lacks an adequate comparison between foil and foam radiators of identical parameters.

Detailed studies of the properties of different foams have been carried out in ref. [56]. The main properties of such foams are listed in table 2. As a reference the

regular radiator (here in after called REG) made of 20 μm polypropylene foils with 280 μm gaps was used.

All radiators were 6 mm thick. Moreover, radiator REG and polyethylene foam with 0.064 g/cm^3 density have the same thickness in units of g/cm^2 . Polyurethane and carbon foams were of special interest because they proved to be rather rigid and exhibit an exceptional radiation hardness [57]. The TR photons were detected by a proportional chamber which contained a layer of 2 mm Xe gas.

The comparison of energy deposition from electrons (3 GeV, $\gamma = 6000$) and pions (3 GeV, $\gamma = 22$) is shown in fig. 21. Each point on fig. 21 corresponds to a certain energy deposition threshold (compare with fig. 17). The abscissa shows the probability to exceed the threshold for pions, and the ordinate that for electrons. Again (as in fig. 17) the "highest" ordinate position of a point for the same threshold gives the best TR yield. The results in fig. 21 are shown for radiators made of foam with optimum densities for each case (with respect to the best TR yield).

The solid curves in fig. 21 correspond to calculations performed for regular radiator (REG) and polyethylene foam (0.059 g/cm^3). The TR yield of the foam is smaller, which is mainly due to the dispersion of the effective pore wall thickness as seen by the particle crossing the surface. The best fit of experimental data for foam radiators corresponds to relative fluctuations of an effective pore wall thickness (as seen by the particle) of $\approx 100\%$. The deterioration of the TR yield observed in large pore radiators (polyurethane, polystyrene, some carbon samples) is basically a result of eventual local density fluctuations in the junctions of the pores. Note that polyethylene does

Table 2
Some properties of tested radiators

Radiator	Bulk density [g/cm^3]	Density [g/cm^3]	t [$\times 10^{-2} \text{g}/\text{cm}^2$]	Mass absorption normalized to polypropylene at $E_\gamma = 5.95 \text{keV}$	Number of crossed surfaces	Mean foil thickness a [μm]	Mean pore size b [μm]
CH_2 polypropylene REG foil	0.91	0.064	3.8	1.0	20	20	280
Polyethylene (CH_2) foam	0.93	0.092	5.5	1.2	41	14	133
		0.064	3.8	1.2	31	13	180
		0.059	3.5	1.2	29	13	195
		0.052	3.1	1.2	26	13	220
		0.035	2.1	1.2	17	13	335
Polystyrene (CH) foam	1.05	0.040	2.4	1.1	12	18	480
		0.110	6.3	1.1	40	15	130
Polyurethane foam	1.1	0.045	2.4	1.4	14	15	410
		0.055	3.3	1.4	45	7	130
Carbon foam	1.7	0.080	3.0	1.05	14	13	420

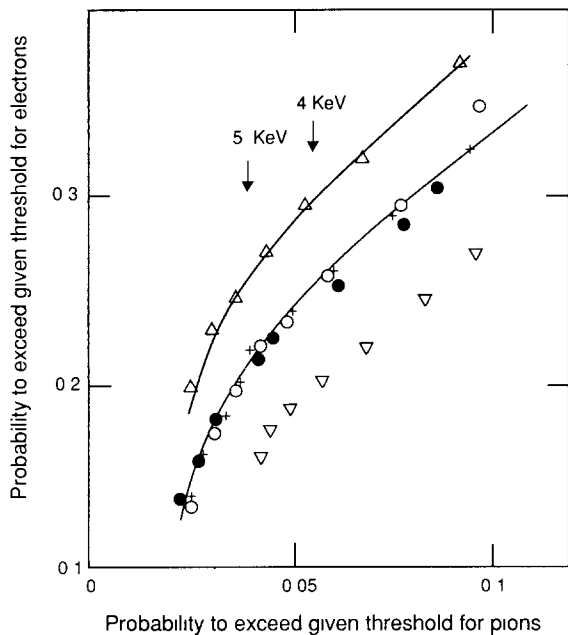


Fig. 21. Comparison of different TR radiators: Δ : regular CH_2 foils; $+$: polyethylene foam, 0.059 g/cm^3 ; \bullet : polystyrene foam, 0.110 g/cm^3 ; \circ : carbon foam, 0.080 g/cm^3 ; ∇ : polystyrene foam with large pore size, 0.040 g/cm^3 .

not have this feature (see fig. 22). The TR yield grows with smaller pore sizes (for all materials except polyethylene), but this implies higher materials density, which means more radiation length the inside TRD ($X_0 = 44 \text{ g/cm}^2$ for CH_2).

4.3. The TR X-ray detector: properties and optimization

The detector observing the TR spectrum emitted from a stack of foils must be sensitive within the energy

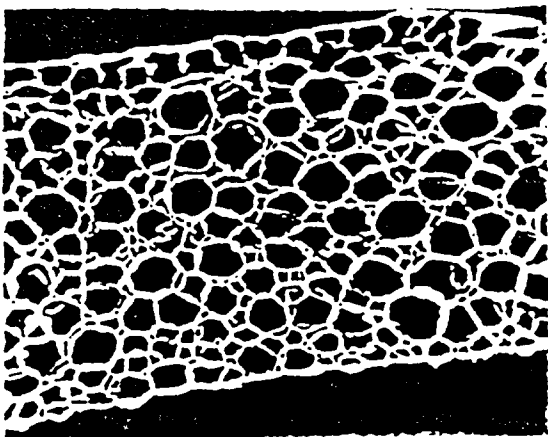


Fig. 22. Microphotograph of polyethylene foam, 0.059 g/cm^3 .

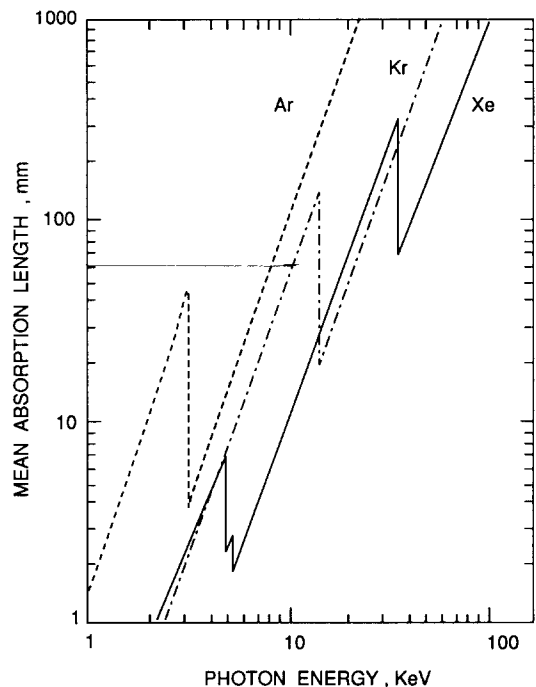


Fig. 23. Mean absorption length of Ar, Kr and Xe.

range from 3 keV to about 30 keV (fig. 19). Since the effective number of foils per foil stack is limited (see fig. 15), it is necessary to use several modules each consisting of radiator and detector in order to obtain sufficient photons from a single particle. The simplest setup consists of a radiator right in front of a multiwire proportional chamber (MWPC) and repeating this several times; this is called the "sandwich array".

The detection efficiency of the MWPC depends on both the geometry (in particular the gas layer) and the gas filling of the chamber. The photon flux absorbed from the primary TR X-ray beam amounts to

$$\alpha = (1 - e^{-l/\lambda}), \quad (25)$$

where l is the thickness of the gas layer and λ the mean absorption length, which is a function of photon energy and the gas filling. λ changes largely with X-ray energy and with the atomic number of the gas. Fig. 23 shows the values of λ for Ar, Kr and Xe, and table 3 contains the X-ray characteristics of these rare gases.

Photon absorption within an atomic shell is followed by either characteristic fluorescence emission or by the ejection of electrons, named Auger emission. The relative probability of fluorescence emission is called fluorescence yield. As a result, the energy of the absorbed photon is converted into either electron-kinetic energy (photoelectron and Auger electrons) or fluorescence X-rays. The ejected electrons may not dissipate all their energy within the chamber gas, and

Table 3
X-ray characteristics of rare gases

Element	Edge $E_{K,L}$ [keV]	Fluorescence yields ^a $\omega_{K,L}$	Edge jump ^b $J_{K,L}$	Weighted averages of line K, L [keV]	Z
Argon K	3.203	0.122	9.91	α 2.96 β 3.19	18
Krypton K	14.323	0.660	7.04	α 12.63 β 14.13	36
Xenon L	4.781	0.103	2.88	4.40	54
K	34.561	0.894	6.08	α 29.67 β 33.76	

^a “Most reliable” experimental values from ref. [58].

^b From ref. [59].

the fluorescence X-rays may not be reabsorbed either, to yield an effective signal. In fact, our MWPC is so thin that all fluorescence and part of the ejected electrons, produced by primary photons, could not be absorbed before reaching the chambers walls.

To estimate the escape probabilities of the fluorescence X-rays we have used the mean free paths for each fluorescence X-ray energy [60] (table 4). The X-ray absorption range of interest (3–30 keV) contains mostly L-fluorescence of Xe (fluorescence yield: 0.103, table 3) and K fluorescence of Kr (fluorescence yield: 0.66). Taking into account the mean free paths for these fluorescence lines we conclude that L-fluorescence X-rays of Xe have an escape probability of $\approx 20\%$ within 1 cm of Xe layer, while K-fluorescence X-rays of krypton escape nearly totally. This is the first argument in favour of xenon gas.

To estimate the fraction of photoelectrons which are not absorbed before reaching the chamber walls,

Table 4
Data for evaluating the fluorescence escape probability

Gas	Density ρ [mg/cm ³]	Fluorescent X-ray energy [keV]	Mass absorption coefficient ω [cm ² /mg]	Mean free path ($\omega\rho$) ⁻¹ [cm]
Kr	3.74	L _{α} 1.587	1.003	0.2666
		L _{β} 1.638	0.9335	0.2864
		K _{α} 12.648	0.02618	10.21
		K _{β} 14.112	0.01914	13.97
Xe	5.90	L _{α} 4.111	0.3692	0.4591
		L _{β} 4.422	0.3087	0.5490
		K _{α} 29.802	0.007971	21.26
		K _{β} 33.644	0.005603	30.25

Table 5
Data for the electron range

Gas in MWPC	Atomic number Z	Atomic weight A	Density ρ [mg cm ⁻³]	Electron range for $E_\gamma = 10$ keV [mm]
Kr	36	83.8	3.74	0.50
Xe	54	131.3	5.90	0.18

we will calculate the electron range which is given by [61]:

$$R \text{ (mg/cm}^2\text{)} = AE(\text{keV}) \left[1 - \frac{B}{1 + CE(\text{keV})} \right], \quad (26)$$

where

$$A = 0.55 \text{ mg cm}^{-2} \text{ keV}^{-1},$$

$$B = 0.9841,$$

$$C = 0.003 \text{ keV}^{-1}.$$

Taking a typical photon energy of 10 keV the ranges of photoelectrons for Kr and Xe gases are given in table 5. The photoelectron energy losses are less in case of Xe: this is the second argument in favour of Xe gas.

The optimum thickness for the detector is approximately one absorption length of TR X-rays at an average energy of about 10 keV; this implies a thickness of about 10 mm for Xe and of about 50 mm for Kr (fig. 23). Since the background for TR photon detection in a MWPC originates mainly from ionization losses of the charged particle, the best chamber gas should yield the lowest ratio of absorption length to the ionization loss of the charge particle in the gas. The TR photon spectrum (fig. 19) has a practical threshold at ≈ 4 keV; for this reason we have to consider the energy losses of the particle in the gas where the transferred energy exceeds ≈ 4 keV (cluster counting method N). Fig. 24 shows calculated results of such losses [62]. The ratio mentioned above can be obtained from figs. 23 and 24 and is better for Xe gas again (a factor of ≈ 1.3). This is the third argument in favour of xenon gas.

For the separation of high energy electrons (with dE/dx already on the relativistic Fermi plateau) and relatively slow hadrons (with an energy of about 1 GeV, i.e. minimum ionizing particles), the considerable contribution to the electron signal is given by the relativistic rise of dE/dx . Fig. 25 shows the relative relativistic rise for different gases [62]. Again xenon looks best. This is the fourth argument to use xenon gas.

The distribution of the number of absorbed TR photons along the path in the xenon gas is shown in fig. 26. As expected, the effective gas thickness is about 10–15 mm. Smaller thicknesses of the xenon gas layer lead to deterioration of the identification capability of

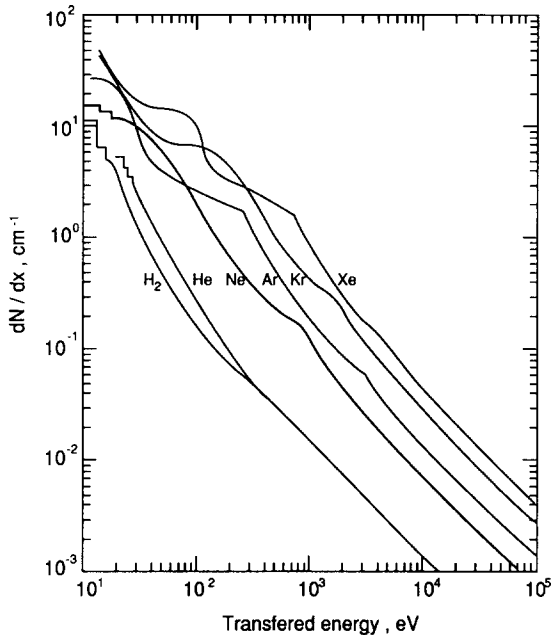


Fig. 24. Probability of relativistic particle collisions with different atoms as a function of energy transferred to an atomic electron.

the TRD because of less efficient X-rays detection. A thicker xenon layer would increase the background due to dE/dx losses. These two facts explain the flat optimum of the π/e rejection power as a function of the xenon gas thickness (HELIOS TRD) in fig. 27.

We already mentioned (see section 4.1) two methods of TR detection:

- total energy deposition (Q); and
- cluster counting (N).

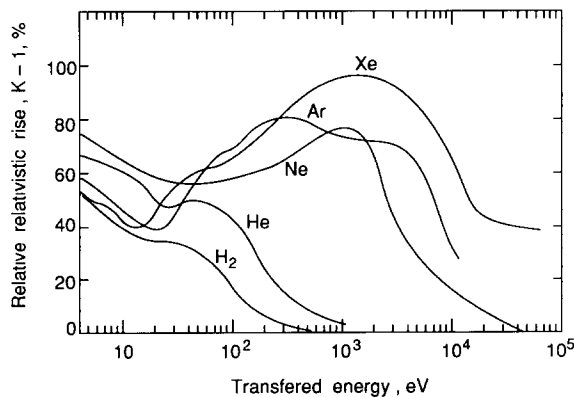


Fig. 25. The relative relativistic rise of energy losses as a function of transferred energy ϵ . The Kr curve has to be located just in between Ar and Xe. K means the ratio dE/dx at the Fermi plateau and at the ionization minimum.

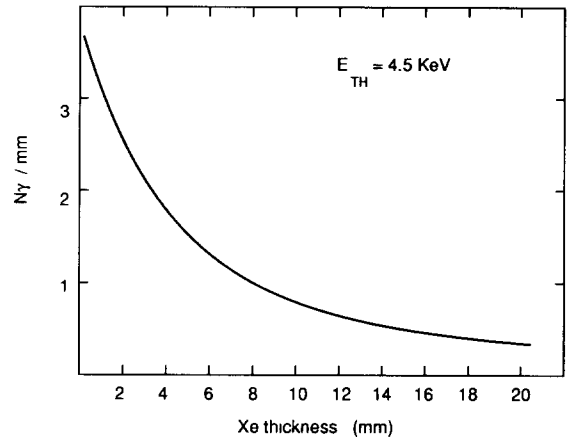


Fig. 26. The distribution of adsorbed X-rays along the path in Xe gas for TR radiator CH_2 (250, 20 μm , 230 μm) (MC calculations).

There are two difficulties in achieving good efficiency of cluster counting (N) connected with the properties of xenon gas:

- 1) The reduction of the gas gain on the anode wire due to the ion space charge (all electrons from the particle track come to the same point of the anode wire for an angle of 90° between particle and anode wire). This is important for the Q-method as well;
- 2) The diffusion of electrons belonging to the cluster during their drift to the anode wire.

The non-linearity in the energy response of a proportional chamber is shown in fig. 28 [71] as function of the gas gain (for a 50%/50% Xe/ CO_2 mixture); up to a gain of $\approx 10^4$ the linearity is good (for a cluster energy up to 6 keV). For the gain exceeding 10^4 the space charge effects become sizeable and lead to a nonlinear response. These space charge effects can be decreased by a rotation of the anode wire relative to the track direction. Fig. 29 shows the increase in the

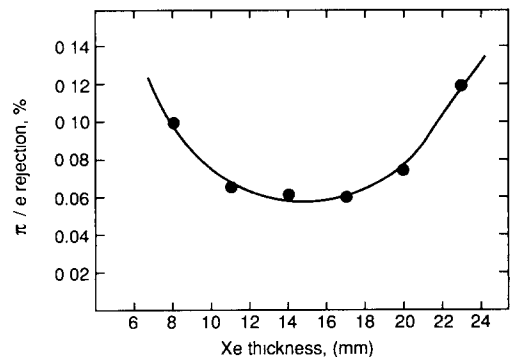


Fig. 27. The π/e rejection as a function of Xe gas thickness in a TR detector. Threshold energy of ionization clusters in gas is 5 keV.

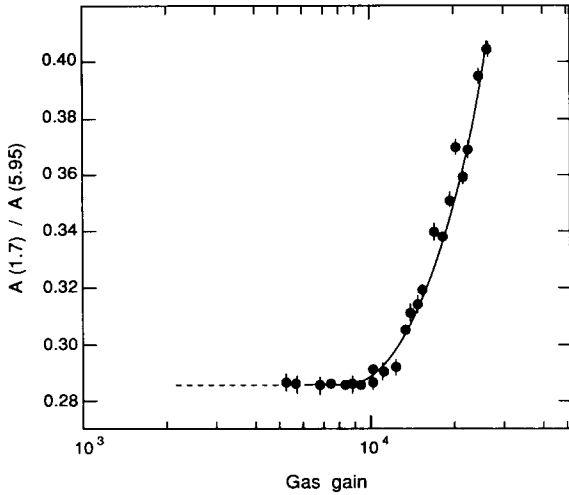


Fig. 28. The ratio of PC signals at 1.7 keV (Xe escape peak) and 5.95 keV (⁵⁵Fe) vs gas (50% mixture of Xe and CO₂) gain.

number of TR clusters from 3 GeV electrons as a function of the angle between track and anode wire; for an angle < 65° the number of clusters is within a few percent compatible with that expected from TR theory.

The diffusion properties of electrons during their drift (1 cm) in xenon containing gases have been measured in ref. [63], (figs. 30a–30d) as a function of electric field. The typical longitudinal diffusion size of an electron cluster drifting in an electric field of about 1 kV/cm ranges from $2\sigma = 500\text{--}600\ \mu\text{m}$ (Xe + CH₄) to $2\sigma = 300\text{--}400\ \mu\text{m}$ (Xe + cooling gas: SO₂ or dymethylether (DME)) for a drift distance of 10 mm. The value of the transverse diffusion of electrons is typically a factor of 2–3 more for these gases and the same electric field [64].

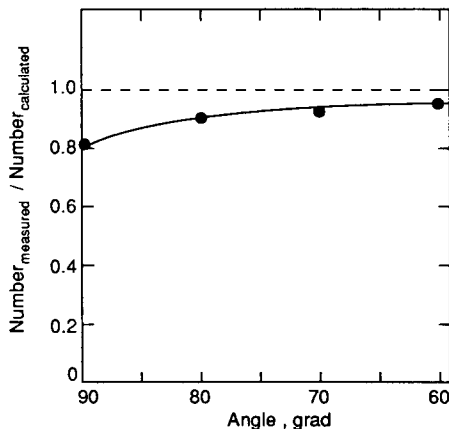


Fig. 29. Ratio of measured and calculated TR cluster numbers, (energy more than 4.5 keV) as a function of the angle between anode wire and particle.

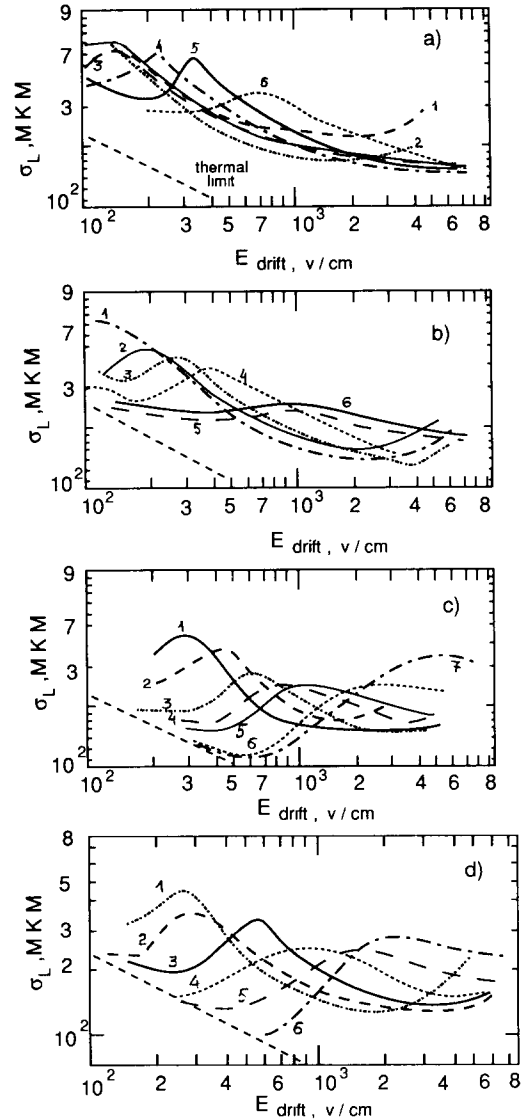


Fig. 30. The longitudinal diffusion of drifting electrons as a function of drift field: (a) Xe–CH₄. CH₄ content: 1) 2%; 2) 4%; 3) 6%; 4) 15%; 5) 20%; 6) 30% (b) Xe–iC₄H₁₀. iC₄H₁₀ content: 1) 2%; 2) 4%; 3) 6%; 4) 10%; 5) 15%; 6) 20%. (c) Xe–CO₂. CO₂ content: 1) 2.5%; 2) 5%; 3) 10%; 4) 15%; 5) 20%; 6) 30%; 7) 40%. (d) Xe–DME. DME content: 1) 2%; 1) 4%; 2) 6%; 3) 10%; 4) 15%; 5) 25%.

In summary, it is difficult to obtain a two-cluster resolution in space better than 2–3 mm [35] because of space charge effects, diffusion of electrons, and the shaping time of the electronics.

The gas mixture to be used in the proportional chambers of transition radiation detectors (TRDs) must:

- i) provide high drift velocities of electrons (in particular for high luminosity colliders);

- ii) contain an optimum concentration of xenon in order to enhance the rejection power of a TRD;
- iii) provide good energy resolution; and
- iv) provide high detector vitality, i.e. suppress aging processes that are mainly due to polymerization on the anodes.

The drift velocities of different gas mixtures have been measured in refs. [63,65] (see fig. 31), for a wide range of gas components and drift fields. Analysis of up-to-date information on electron drift velocities in Xe-containing mixtures (see also refs. [66–68] as well as information on ageing problems [69,70], allow us to select two molecular admixtures – CO_2 and CF_4 – as the most promising candidates (see figs. 31d and 31e). The mixture based on Xe/CO_2 ($\approx 50/50$) exhibits a high drift velocity ($\approx 60\text{--}70\text{ mm}/\mu\text{m}$ for high electric fields), good energy resolution (22% FWHM for a ^{55}Fe γ -source of 5.95 keV), and good quenching properties. A Xe/CF_4 mixture is even faster, but has worse energy resolution [65]. The values of the charge dose, after

which the chambers show signs of ageing, are [69,71] $> 2\text{ C}/\text{cm}$ for Xe/CO_2 and $\geq 5\text{ C}/\text{cm}$ for mixtures with CF_4 .

4.4. Geometries of TR gas detector

Different geometries of TR chambers have been used:

1) The conventional MWPC (see, for example refs. [19,39,50,72–75,77]). Usually the total thickness of Xe (Kr) gas is 10–30 mm, the pitch between the anode wires is 2–5 mm.

2) The radial drift chamber [76] (see fig. 32) was proposed for the forward track detector of H1. Such a chamber design results in efficient X-ray detection and track reconstruction, and good accuracy.

3) To achieve the best electron/pion discrimination we have to use many modules with rather thin radiators and correspondingly frequent measurements of the TR photon [35] (see below). Straw chambers cm-

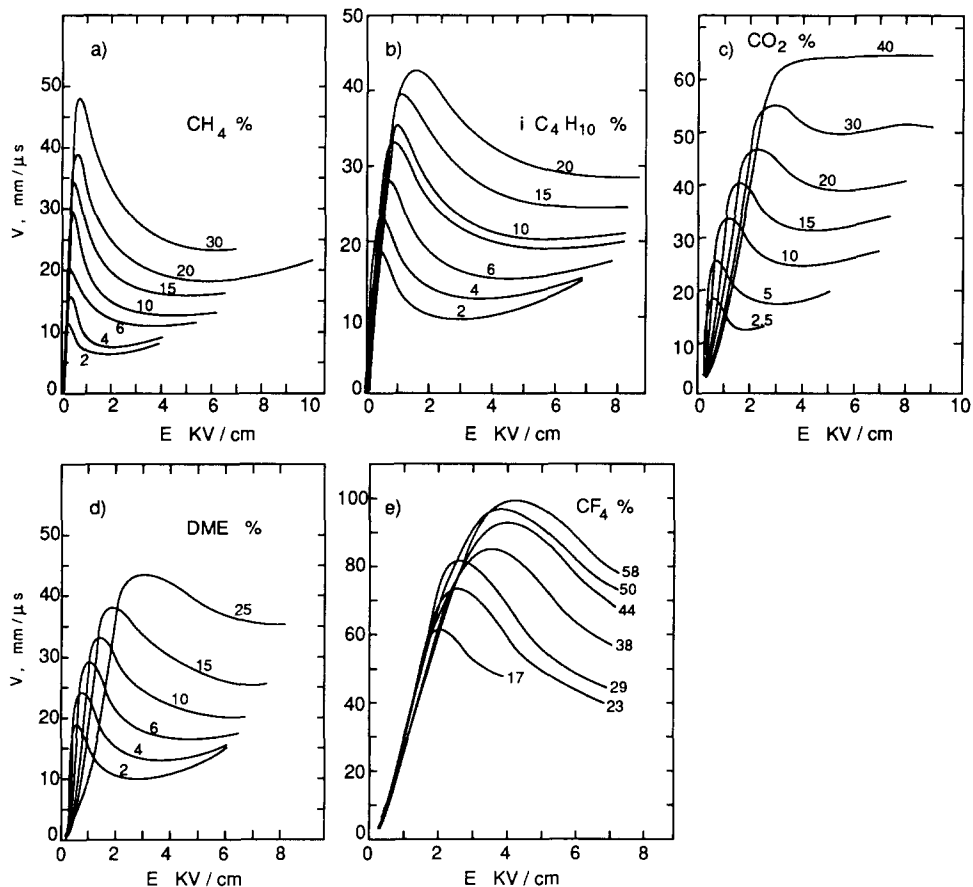


Fig. 31. Drift velocities of electrons for different gas mixtures; the numbers are molecular admixtures (%): (a) $\text{Xe}-\text{CH}_4$; (b) $\text{Xe}-i\text{C}_4\text{H}_{10}$; (c) $\text{Xe}-\text{CO}_2$; (d) $\text{Xe}-\text{DME}$; (e) $\text{Xe}-\text{CF}_4$.

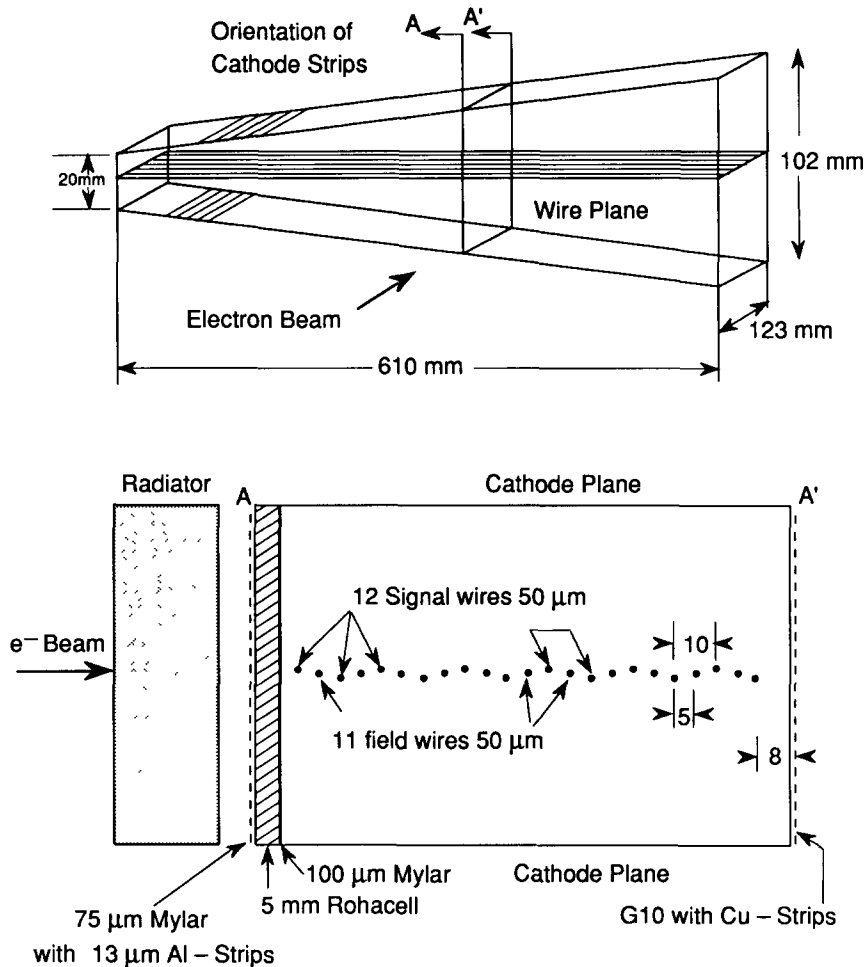


Fig. 32. The geometry of the single wedge prototype radial drift chamber.

bedded in foam radiator are proposed as X-ray detectors for high luminosity colliders (TRD tracker concept [71]).

4) The longitudinal drift chamber [35,45,51,78] is more suitable for the cluster counting technique (fig. 33 [45]). In this case the ionization due to X-ray photoabsorption in the gas of the MWPC is concentrated in a small space; the size of this ionization cluster is mainly defined by the diffusion of electrons drifting through the gas ($\approx 500 \mu\text{m}$ FWHM, fig. 30). The only background for TR detection results from δ -rays of a few keV produced by ionizing particles. The formation of these δ -rays is Poissonian distributed.

The longitudinal drift chamber (fig. 33) has a drift space of typically 10 mm and an anode space of about 6 mm, which result in a total drift time of $\approx 0.5\text{--}1 \mu\text{s}$. The detection of ionization clusters is provided by FADC (fig. 33, lower part) or by discriminators and scalers [35].

Gas purity is required because of attachment problems. To obtain electron lifetimes greater than $100 \mu\text{s}$, for instance, one asks for less than 160 ppm of oxygen for any xenon filled detector [79]. These are not exclusively stringent requirements, except that xenon is very expensive, so that users must recirculate the gas (see for instance, ref. [73]), rather than to waste it by single through-flow [35,39].

Because of the soft part of the TR spectrum, the entrance window of the chamber should be very thin and should have a low average atomic number (typically $20\text{--}40 \mu\text{m}$ of mylar). The "hydrostatic" pressure inside the chamber due to the high density of the xenon gas, which is four times heavier than air, causes thin windows to sag, and chamber uniformity suffers if the windows deform the cathodes of the detector. This problem becomes important for window dimensions larger than about 50 cm. Various solutions to this problem have been found. The HELIOS TRD (see

below) uses a double window (see fig. 34) to rectify the exit cathode; in the EHS TRD the xenon was deluted with four parts of helium, to obtain a chamber gas with the same density as air; the sensitive volume of the E715 TRD (70% Xe + 30% CH₄) was surrounded by two “compensating” volumes [39] filled with CO₂ at a pressure sufficient to keep the cathode planes parallel to the anode plane.

4.5. The “fine grain” structure and compact TRDs

In colliding beam experiments the space available for the TRD is limited (typically about 50–100 cm). This leads to limitations for the gaps between the radiator foils (optimum gap value is about 200–300 μm, see fig. 18). For a 200–250 μm foil within for one TRD module, the radiator block has to be about 70 mm long (like the HELIOS TRD). Adding the optimum thickness of the TR chamber (about 15 mm of xenon) results in a typical length for one module of 85–90 mm.

For the total energy deposition method of TR detection (Q-method) the main source of background for TR X-rays is a very broad distribution of ionization

loss; this distribution was calculated in detail for different gases in ref. [62]. In the case of the cluster counting (N-method), the source of background are δ-rays with energies exceeding the threshold of cluster counting ($E_{TH} > 4-5$ keV). They are Poisson distributed. More exactly, this background includes also the number of ionization clusters in xenon gas having an energy deposition of more than the threshold energy E_{TH} within a certain small space volume. This volume is determined by the drift velocity of the electrons, the geometry of the electric field in the chamber, and by the shaping time of the electronics used for cluster detection. Fig. 35 shows the probability of energy depositions exceeding E_{TH} for relativistic particles in xenon gas [80]. Note, the nonlinear behavior between probability and gas thickness. From fig. 35 follows, that the size of the detected ionization clusters should be as small as possible in order to decrease the background of the dE/dx clusters. This is particularly important for the rejection power of many hadrons against electrons in the case of nonisolated electron identification (see below). For drift velocities of about 50 mm/μs for xenon containing mixtures (fig. 31) the detected ionization clusters of

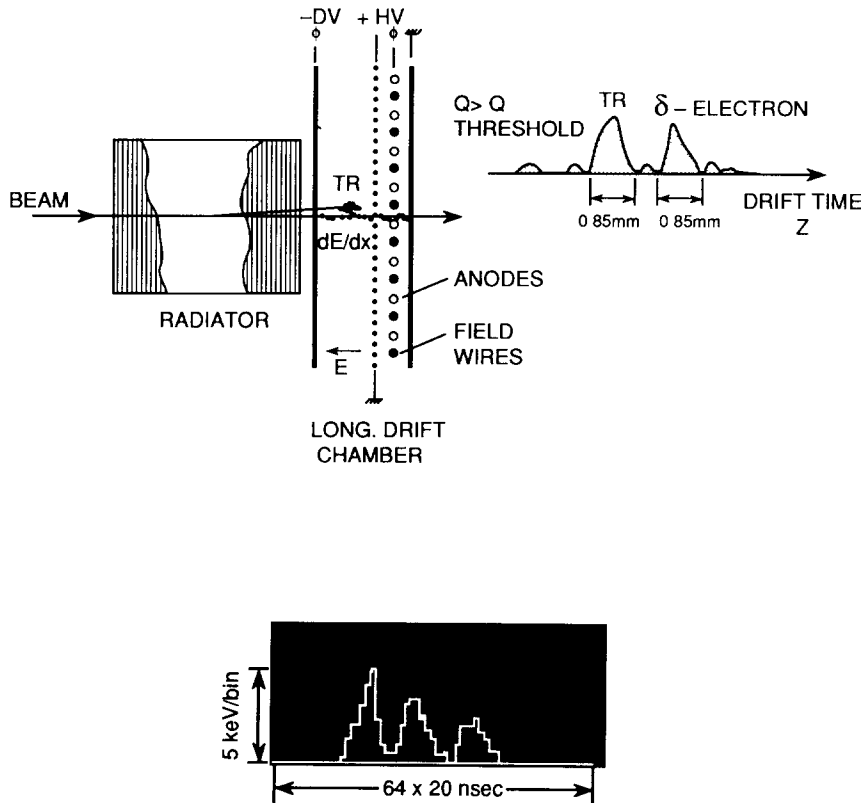


Fig. 33. The longitudinal drift chamber concept. It is more suitable for the cluster counting technique. The lower part of the figure presents the FADC signal of such a TRD.

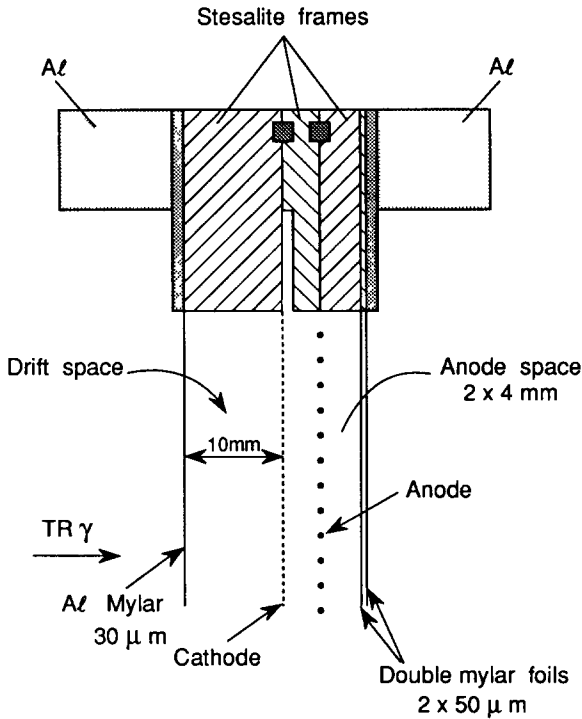


Fig. 34. The design of HELIOS TR chamber with the double cathode window: the internal window is flat; the sag of the external window does not influence the uniformity of the cathode-anode field.

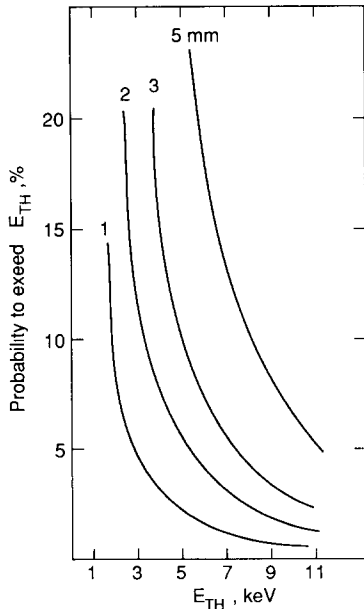


Fig. 35. Probability to exceed the threshold energy E_{TH} for Xe gas layers of different thickness by relativistic particles (Fermi plateau).

≈ 1 mm size require an electronics shaping time of about 10 ns. The threshold energy E_{TH} of the clusters has a broad optimum between 3 and 6 keV (figs. 36a [45] and 36b). The difference of optimum E_{TH} values for Li and CH_2 radiators is due to the softer TR spectrum for the Li-radiator.

As already mentioned above, the TR radiation ability A_{TR} (detected photons/cm of a TRD) is small ($\approx 0.1-0.2$ photons cm^{-1}) and the rejection power depends very strongly on A_{TR} . A_{TR} [35] can be increased by subdividing each radiator-detector module into many small modulus, but conserving at the same time the total thickness of the radiator. Fig. 37 gives the results of such a "fine grain sampling approach". With this approach the TR radiation ability can be considerably increased and the e/π rejection power is about 20 times improved. One module of such an optimized fine grain TRD consists of:

- radiator: $17 \mu m$ CH_2 foils, spaced by $250 \mu m$;
- number of foils $\approx 40-60$;
- xenon gas thickness $\approx 2-4$ mm.

These TRD parameters match the threshold energy $E_{TH} = 4.5$ keV of detected X-rays well.

This TRD type represents in fact a modification of the cluster counting device (N), if each detector with 2

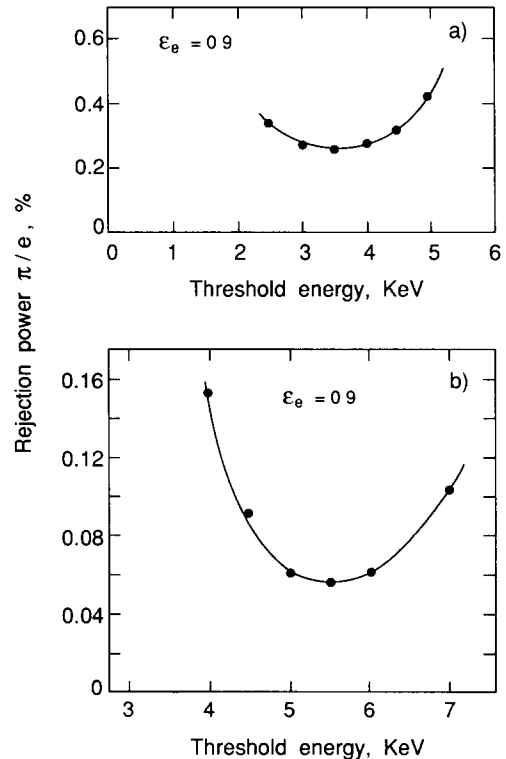


Fig. 36. Rejection power optimization as a function of cluster threshold energy: (a) Li foils radiator. (b) CH_2 foils radiator.

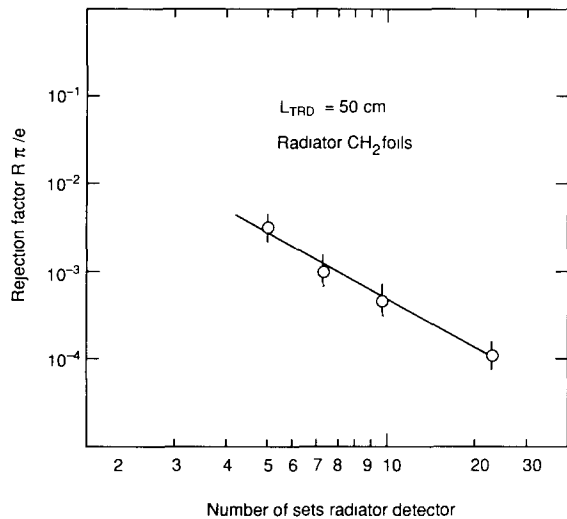


Fig. 37. Optimization of $\text{CH}_2 + \text{Xe}$ "fine grain" TRD: this figure provides a fast choice of the TRD structure.

mm xenon gap works in digital mode and therefore the number of fired ($\geq E_{\text{TH}}$) detectors follows a binomial distribution.

5. The application of TRDs in HEP experiments

In high energy experiments the observation of transition radiation can provide valuable *nondestructive* information for particle identification, which is both complementary and supplementary to calorimetric measurements.

The physics requirement for the TRD is to augment the electron identification ability of a fine grained calorimeter, essentially in jetlike multiparticle events. Background particles are charged pions, which generate a charged track, matching e.m. energy deposition in a calorimeter by neutral pions.

The identification of hadrons (pions against kaons and protons) by TRD is limited (see below) and elec-

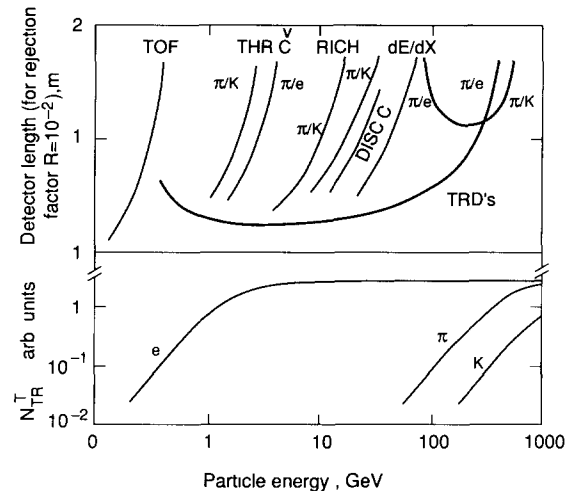


Fig. 38. Particle identification by different methods for compact optimized (< 1 m) detectors. Upper part: length of different detectors needed to achieve 10^{-2} of rejection power. Lower part: the transition radiation intensity vs energy of the particles.

tron identification is the most promising application of TRDs in accelerator experiments. Fig. 38 illustrates the region of TRD application on the energy scale among other detectors for particle identification. The detector length needed to achieve the rejection factor $R = 10^{-2}$ (for a definition of R , see section 4) is shown as a function of particle energy on the upper part of fig. 38. The lower part demonstrates the threshold character of TR, which is saturated for Lorentz factors $\gamma = E/mc^2 \geq 5 \times 10^3$. This saturation is typical for the relatively small length of a compact TRD, due to the limitation of the gaps between the radiator foils ($\approx 200 \mu\text{m}$). Fig. 38 shows the wide energy interval between the thresholds of TR photon production by electrons (≈ 1 GeV) and by pions (≈ 150 GeV). The corresponding π/K interval is too narrow and this is a reason for limited pion-kaon (proton) identification by a compact (≤ 1 m) TRD.

Table 6
TRD used for e/π separation

Experiment Ref.	R806 [19]	E715 [39]	NA34 (HELIOS)	UA6 [77]	UA2 [78]	E769 [75]	NA31 [73]	NA24 [84]	VENUS [72]	ZEUS [81]	H1 [76]	DØ [51]
Length [cm]	55	360	70	55	22	130	110	60	30	56	50	32
N modules	2	12	8	3	2	24	4	4	4	4	3	3
Radiator	Li	CH_2	CH_2	Li	CH_2							
Method	Q	N	N	Q	FADC	N	Q	N	Q	FADC	FADC	FADC
Rejection R [%]	5	0.06	0.05	10	8	2	10	0.5	3.5	2	4	2
Efficiency for light particles [%]	90	99	90	90	80	87	98.7	80	90	90	90	90

5.1. Examples of TRDs in HEP experiments

Some typical TRD applications are shown in table 6. The first eight experiments listed in the table have already taken data and produced physics results. The remaining four TRDs are currently being tested in their final location.

5.1.1. E715 transition radiation detector [39]

The experiment E715 detected 90 000 beta decays $\Sigma \Rightarrow ne\nu$ of polarized hyperons within the 1000 times more copious background reaction $\Sigma \Rightarrow n\pi$. The last reaction had to be suppressed by at least 4 orders of magnitude by maintaining a high detection efficiency for hyperon beta decays. This goal was achieved by using a TRD followed by a lead glass calorimeter. The detector consisted of 12 identical modules, each containing a radiator (210 layers of 17 μm polypropylene foils separated by 1 mm each) and a MWPC (anode-cathode distance of 8 mm, anode pitch of 2 mm). The electron collection time of the MWPC (Xe/CH_4 , 70/30) was 300 ns.

The experiment had 3.6 m space available for the TRD; therefore it was a “noncompact” detector. The cluster counting (threshold energy 6.5 keV) method (N) was used and every eight subsequently adjacent anode wires were connected together. The γ -dependence of the measured cluster numbers is shown in fig. 12. The extremely good off-line rejection factor $R_{\pi/e} = 6 \times 10^{-4}$ was obtained with an electron efficiency of 99.5%, for isolated particles. The distributions of cluster number for electrons and pions are shown in fig. 39. As a result, the sample of electron candidates, selected by both the calorimeter and the momentum measurement

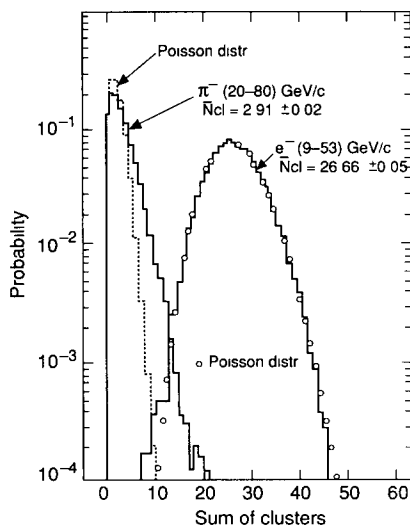


Fig. 39. The cluster distributions for electrons and for pions, E715 TRD [39].

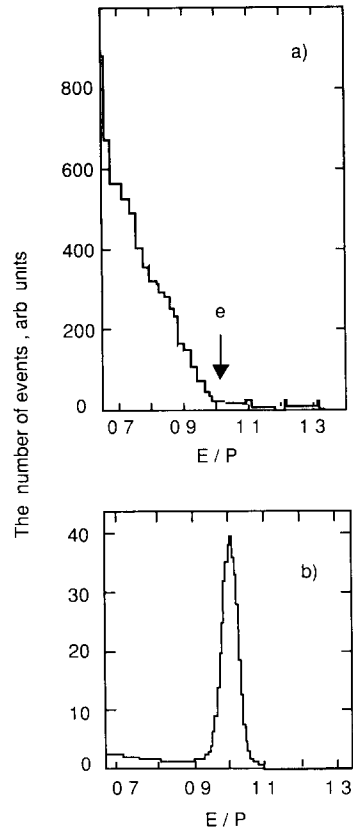


Fig. 40. Histogram (a) shows E/p distribution of all charged particles in experiment E715; (b) shows the same distribution for particles identified as electrons by TRD.

was “cleaned” by TRD very impressively (fig. 40). The E715 TRD performance was disturbed by interactions of incident particles (pions from $\Gamma \Rightarrow \pi n$ decays) in radiator material (a few g/cm^2). Therefore, only a rejection factor $R = 2.5 \times 10^{-2}$ was achieved online.

The best way to reject these particle interactants at the trigger level involves detailed track information and detection of TR X-rays just along the track.

5.1.2. A high rate TRD for particle identification in hadron beam (E769) [75]

A TRD was built to separate pions from kaons and protons in the incident 250 GeV/c charged hadron beam for the experiment E769 at Fermilab. This is the first reported use of a TRD for beam particle identification in a running experiment, although several authors have demonstrated the ability to separate pions from heavier hadrons in test beam at similar energies using a prototype TRD [40,44,85,86]. The E769-TRD is a tagging element, working together with a DISC Cherenkov Counter. They tag at a high rate (≈ 2 MHz) the pions in the beam, which was composed of 59% pions, 35% protons and 6% kaons. The TRD con-

tained 24 modules (one module can be seen in fig. 41), each consisting of radiator and two MWPC planes (cathode–anode spacing of 3.175 mm) with an active area of 7.62 cm². The total material exposed by the TRD to the beam corresponded to 8.3% interaction lengths or 16.9% radiation lengths.

Fig. 42 displays the distributions of the number of MWPC planes hit per event for DISC tagged pions and protons. At 87% efficiency for pions the achieved hit number discrimination results in a 2% proton contamination for TRD tagged pion sample.

5.1.3. HELIOS (NA34) transition radiation detector [35,87]

HELIOS (High Energy Lepton and Ion Spectrometer) [88] is an experiment to study lepton production in proton–nucleus collisions, at large solid angle, by efficient detection of electrons, muons and neutrinos (via missing energy and momentum determination). To select the prompt leptons, an extremely high electron identification is needed. For electron identification both a fine grained liquid argon calorimeter and a TRD are used, together with momentum measurements by high precision drift chambers in a magnetic field.

The HELIOS TRD is the first example, where transition radiation detectors are used at the same time as track detectors. The TRD consists of eight radiator–detector modules with anode and cathode strips readout for each of the eight chambers. It applies the cluster counting (N) method for the identification of electrons with energy above 5 GeV. The anode and cathode pitches are different for each module to achieve back pointing to the small (50 μm) target. The electron correlation logic allows one to use for the electron trigger the information about space correlations between energy deposition in the electromagnetic calorimeter, anode and cathode strip sectors of the TRD, and finally the silicon pad detector just

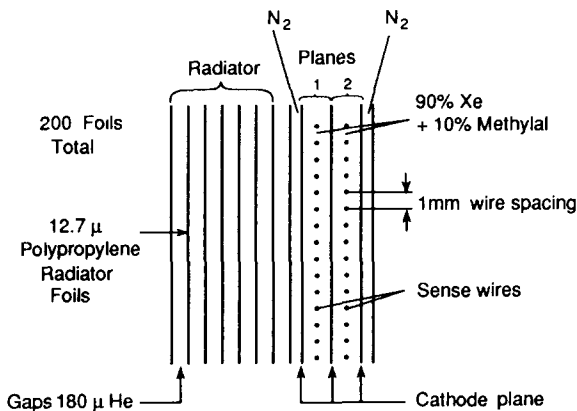


Fig. 41. Schematic of a TRD module in experiment E-769.

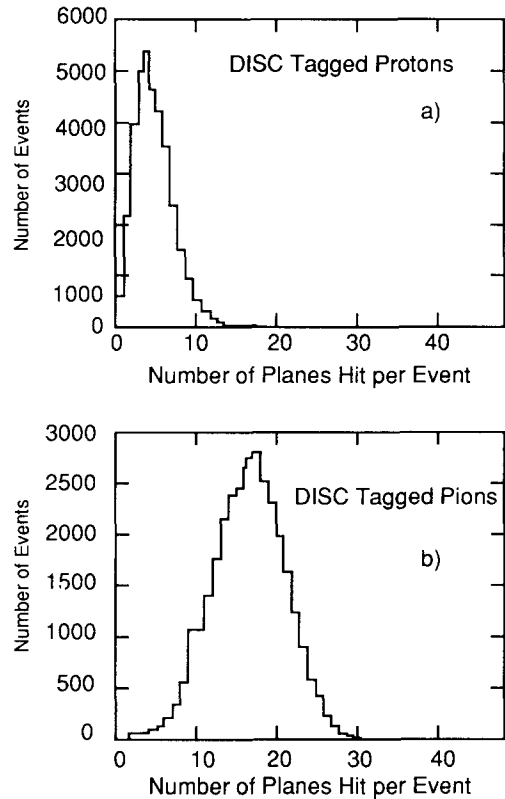


Fig. 42. Number of TRD planes per event that registered hits for a sample of DISC tagged (a) protons and (b) pions.

behind the beam target. The silicon pads allow one to reject the electron–positron pairs, due to gamma-conversions and Dalitz-decays of π^0 , and η . The total electron identification ability in HELIOS for isolated particles should be better than 10^{-5} ($\approx 10^{-2}$ by the calorimeter and $\approx 10^{-3}$ by the TRD). The total length of the TRD is 70 cm, and its fiducial volume is within a cone of ± 100 mrad (at its end section ≈ 70 cm in diameter). Each of the eight polypropylene (PP) radiators of the TRD consist of two parts: one, located just in front of the chamber with 150 foils, 20 μm thick and 250 μm spaced, produces a soft TR spectrum. The other one, located in front of this part with 100 foils, 30 μm thick and 170 μm spaced, emits a harder TR spectrum. The total thickness of the PP foils is 4.5 g/cm². Each of the eight chambers consists of an anode space (2×4 mm) and a drift space (10 mm). It contains 156 anode wires (pitch from 2.3 mm to 2.8 mm) and 62 cathode strips (see fig. 34). The total drift time is 760 ns (620 ns in drift space). The gas gain is 1.5×10^4 with a uniformity of 7% rms. The gas composition is 95 parts Xe and 5 parts is C₄H₁₀.

The use of the HELIOS TRD as a track detector (except for the three sets of the special drift chambers

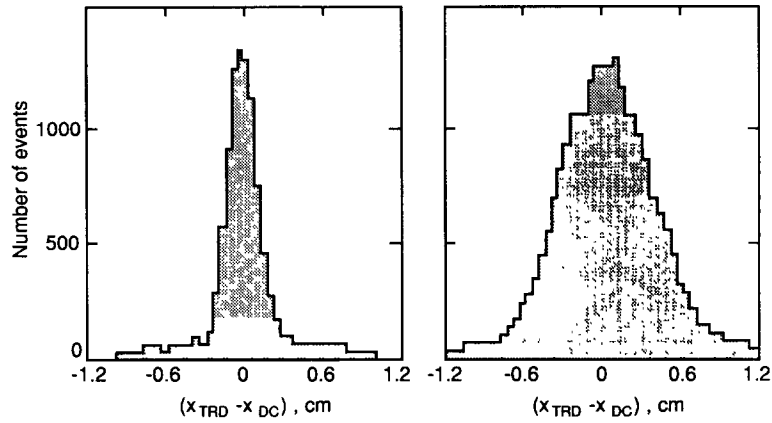


Fig. 43. The track coordinate difference between the high precision drift chambers measurements and off-line tracking by TRD (HELIOS) for anodes (left) and cathodes.

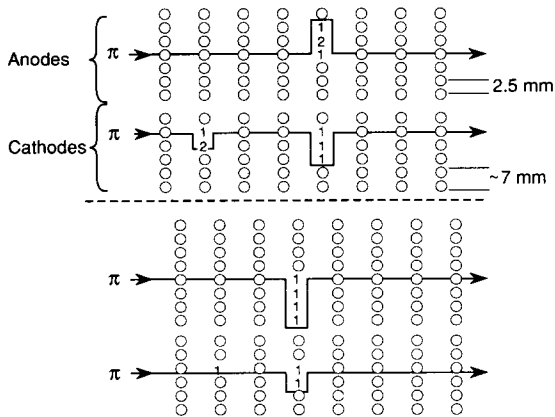


Fig. 44. Raw events from the HELIOS TRD. The eight vertical columns show the number of clusters for each anode (above) and cathode strips (below) of eight chambers. The δ -rays are clearly seen.

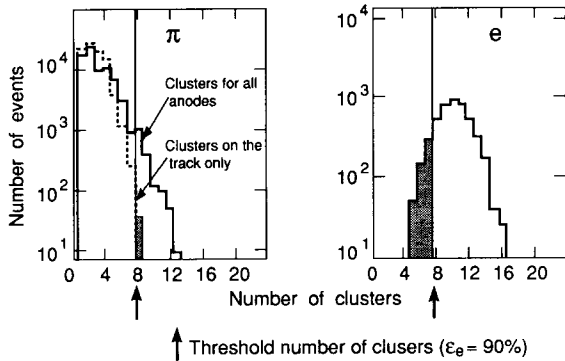


Fig. 45. The frequency of cluster numbers for pions and electrons in the (HELIOS TRD). The full line corresponds to the cluster distribution without δ -ray restriction and the dotted line with restriction.

in front of and behind the TRD) is important for two reasons:

1) Already at the trigger level it serves as a good pointer from the electron track in the TRD into the cluster of electromagnetic energy deposition in the liquid argon uranium calorimeter (ULAC) just behind the TRD. The ability of the HELIOS TRD for electron tracking can be seen in fig. 43, which shows the coordinate difference between electron tracks in the TRD MWPSs and the reconstructed off-line tracks from drift chambers.

2) To suppress long range δ -rays from pion tracks and secondary particles from interactions in the TR

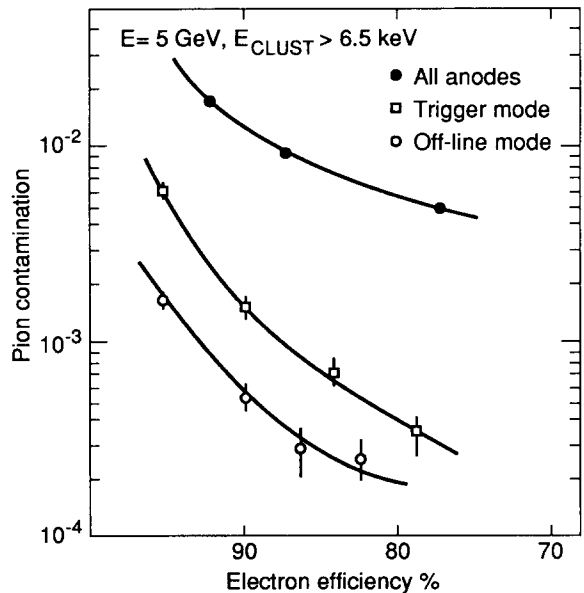


Fig. 46. Rejection power of the HELIOS TRD for different methods of analysis.

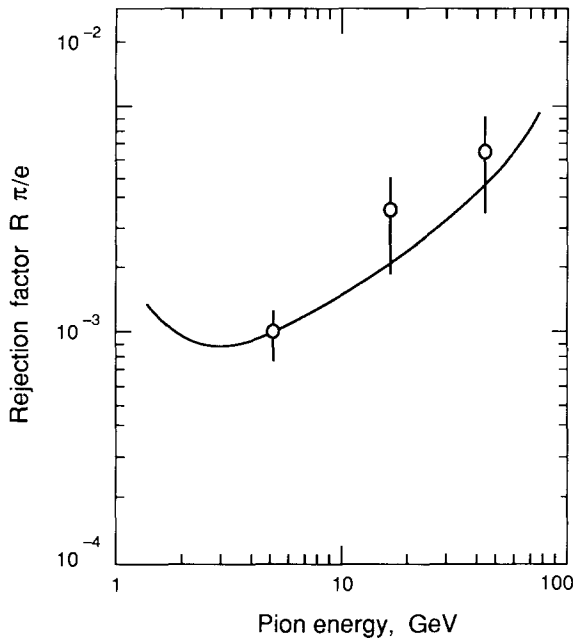


Fig. 47. Energy dependence of the rejection power $R_{\pi/e}$ (HELIOS TRD). The solid curve presents the expectation of TR theory, normalized at 5 GeV.

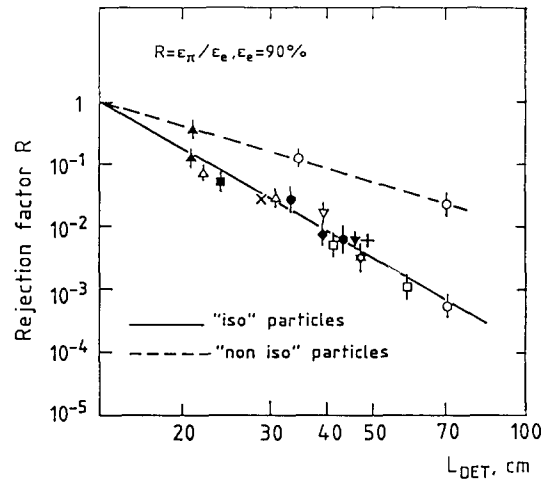


Fig. 48. Pion rejection capabilities of various TRDs versus TRD length: isolated particles [19,35,45,48,50,51,72,73,76,78, 81,82], non-isolated particles [35,78].

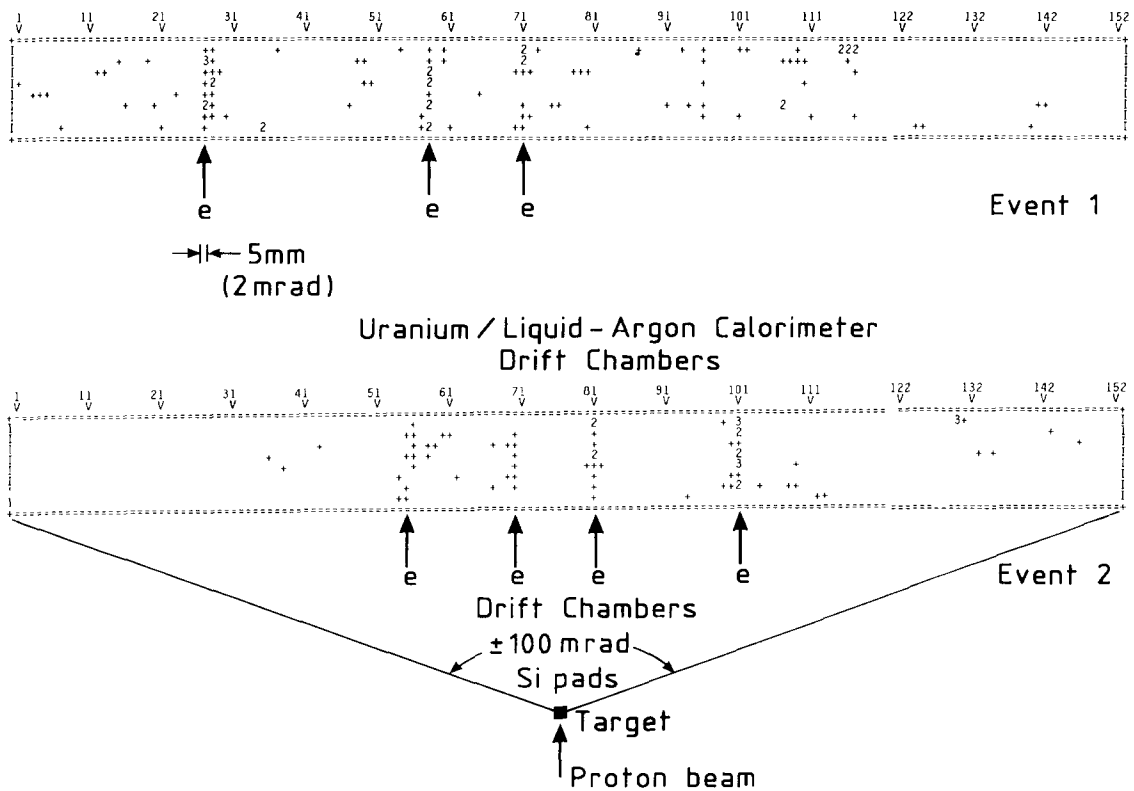


Fig. 49. Display of two events in the HELIOS TRD. The dead space in the TRD is ± 13 mrad around the beam.

radiator material, we restrict cluster counting to the narrow road close to the track, e.g. within the road that includes 1–2 anode (cathode) wires (strips). Examples of such δ -rays on the pion track are shown in fig. 44. The long range δ -rays contribute to the Landau tail of the dE/dx distribution or produce a non-Poissonian

tail of the cluster distribution, if they exceed the two-cluster resolution of the TR chamber (typically 2–3 mm) (see fig. 45). In both cases the energy of the δ -rays is more than approximately 30 keV, and the probability of their production is at the few percent level. This level will determine the rejection power of the TRD

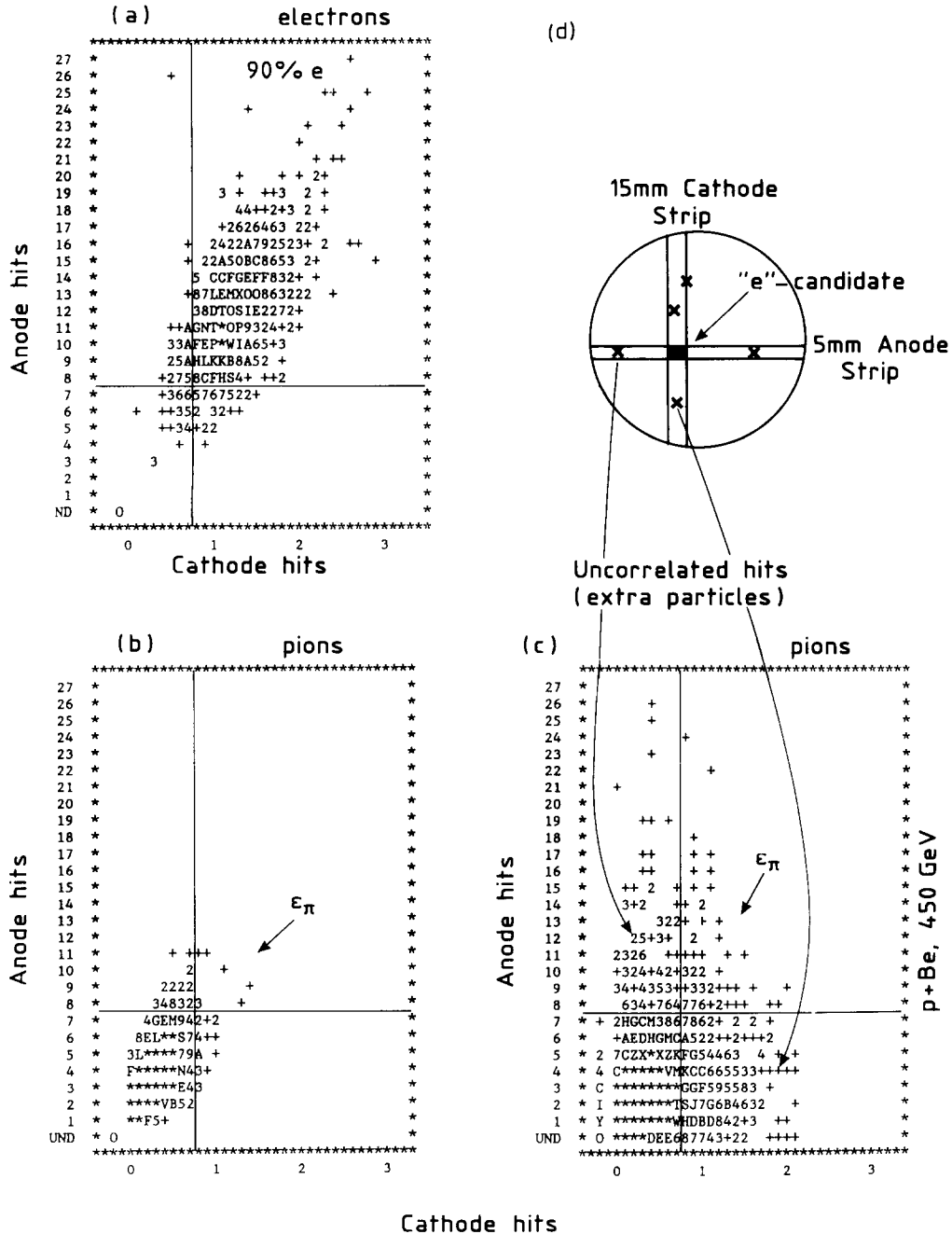


Fig. 50. Scatter plots (anode hits versus cathode hits) for isolated electrons (a), isolated pions (b) and pions inside secondaries produced by p + Be interactions (c). The straight lines correspond to 90% electron efficiency (upper left-hand section).

Table 7
Rejection power of HELIOS TRD ($\times 10^{-3}$) for isolated particles

Cathodes	Mode ^a	Anodes	
		1 anode	2 anodes
1 cathode	1	1.1 ± 0.2	1.4 ± 0.2
	2	0.7 ± 0.2	0.8 ± 0.2
	3	0.5 ± 0.1	0.5 ± 0.1
2 cathodes	1	2.0 ± 0.3	1.5 ± 0.2
	2	1.4 ± 0.3	1.8 ± 0.3
	3	0.9 ± 0.2	0.9 ± 0.2
Without cathodes	1	3.9 ± 0.8	2.8 ± 0.4

^a 1: trigger mode; 2: cluster counting (N) on the track; 3: likelihood method, off-line.

using the clusters which are counted for all anodes (cathode) of each chamber (fig. 46). In fig. 46 the rejection power for cluster counting on the particle track only is also shown for two cases:

a) The two-dimensional analysis on the scatter plot of anode clusters and cathode clusters (figs. 50a and 50b). This method selects the event for $N > N_{\text{anode(cathode)}}^{\text{threshold}}$ and was used for a fast triggering ($\approx 1 \mu\text{s}$).

b) A maximum-likelihood method, using the distribution of probabilities that a given event belongs to electrons or to pions. These probabilities are calculated using two-dimensional scatter plots (like figs. 50a,

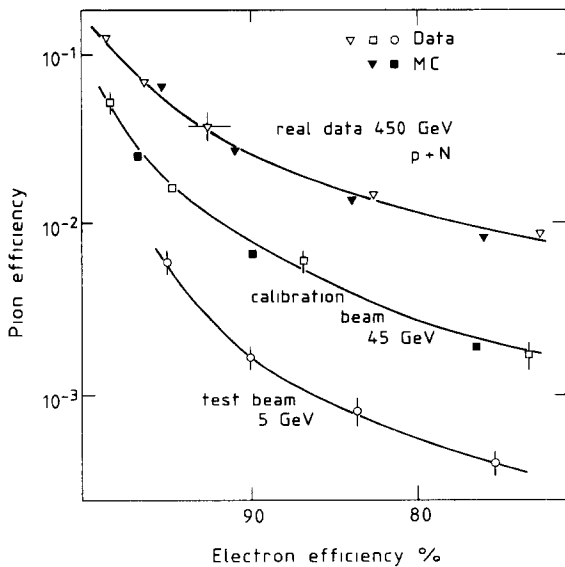


Fig. 51. Pion suppression of the HELIOS TRD under different conditions.

50b) for electrons and pions for each chamber. This method can be used for off-line analysis only.

The results of fig. 46 have been obtained with 5 GeV test beam and include a possible interaction of pions in the radiator material.

The rejection power can be obtained by means of cluster counting using the closest one or two anodes and cathodes to the track. With one anode (cathode) road along the track was lost about 20% of the clusters owing to cluster sharing between neighbor anodes (cathodes) and worsening the rejection power. Table 7 demonstrates all these possibilities for three methods of analysis: 1) trigger mode ($N_{\text{a(c)}} > N_{\text{a,c}}^{\text{THR}}$); 2) $\Sigma ((N_{\text{a}} + N_{\text{c}}) > N_{\text{a+c}}^{\text{THR}})$; 3) likelihood method (mentioned above).

The results of table 7 have been obtained by using an intelligent threshold on the cluster energy, which varied continuously during the drift time. In this way, the intelligent threshold follows the TR cluster energy distribution (4–7 keV) from the chamber entrance (long drift time) to the anode space (short drift time).

Fig. 47 shows the rejection power $R_{\pi/e}$ of the HELIOS TRD as a function of pion energy measured in test- and calibration beams at 5, 17 and 45 GeV. These results have been obtained using only the drift space in the TR chambers (see fig. 34). Theoretical

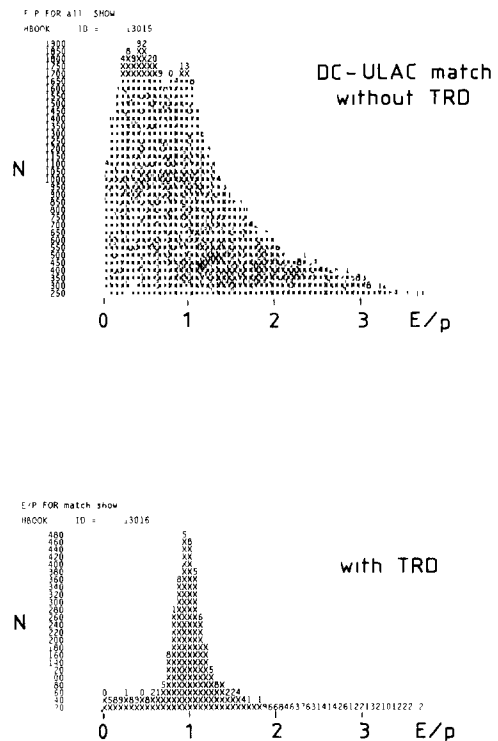


Fig. 52. Cleaning of electron candidates as seen without TRD (a) and with the HELIOS TRD (b) in p+Be interactions.

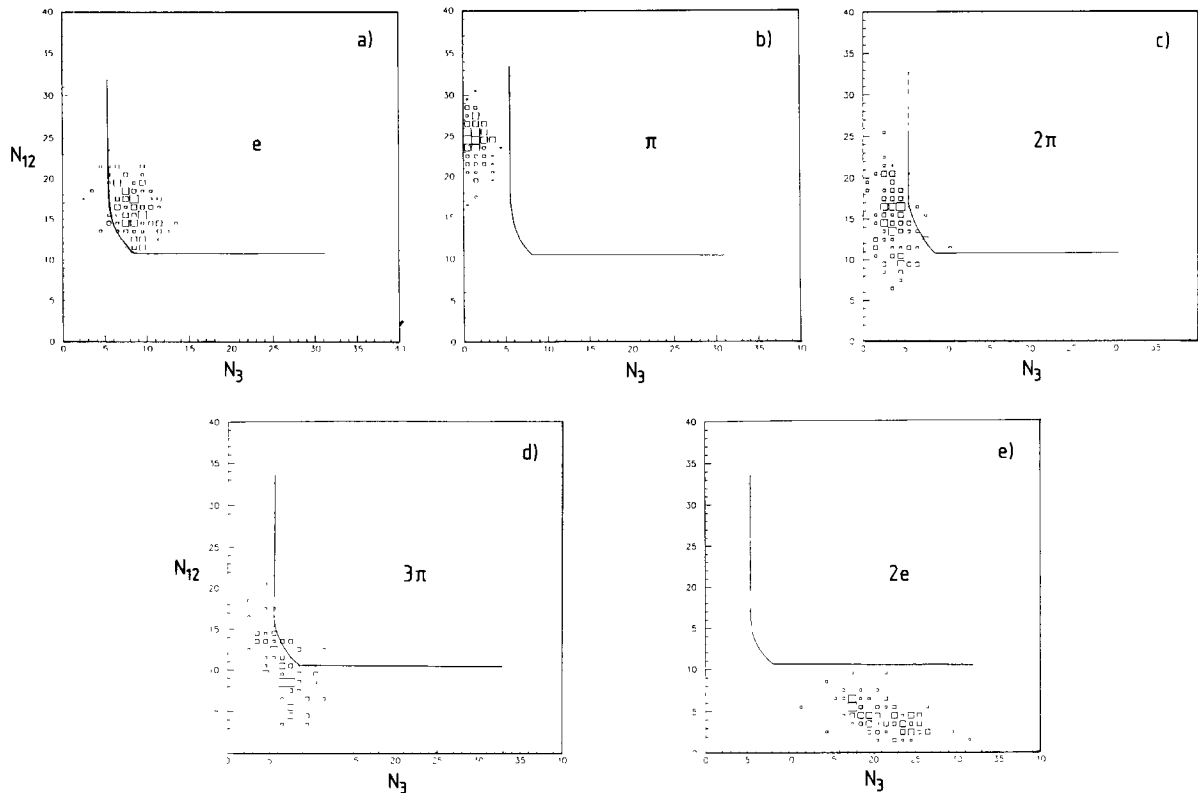


Fig. 53. Scatter plot of the number of fired straws for an energy deposit between the first threshold TH1 and the second one TH2 (N_{12}) vs the corresponding straws number exceeding TH3 (N_3). The distribution for 30 GeV electrons is shown in (a) and in (b) for 10 GeV pions. In (c) and (d) the plots for two π s and three π s respectively are displayed; in (e), the distribution for two overlapping electrons (e.g. from conversion) is shown. The solid lines indicate the area for 90% electron efficiency. The abscissas indicate the number of straws. The mean value of crossed straws is 40.

predictions (solid curve) are normalized at the 5 GeV value, taking into account the relativistic rise of dE/dx for pions.

5.2. The identification of isolated particles: summary

A summary of the experimental results for electron identification is shown in fig. 48 as a function of TRD length. The results are presented for Li and CH_2 radiators and also for different methods of analysis (Q and N). The pion rejection factors obtained at different experiments agree satisfactorily over 2.5 orders of magnitude within a wide range of the total length of the TRD and also for different analytical methods and radiators. For isolated particles a rejection value $R = 10^{-2}-10^{-3}$ can be achieved for a TRD length ≥ 50 cm.

The following conclusions can be drawn from fig. 48:

a) The TRDs using Li or CH_2 radiators have a similar rejection power for a given total lengths;

b) There is no difference in rejection power between the total energy deposition method (Q) and cluster counting method (N).

5.3. The TRD as electron identifier for a high density of secondaries

The TRD rejection power is quite different when the density of secondaries is high (upper curve in fig. 48). Fig. 49 displays two events from the HELIOS experiment (p-Be collisions, 450 GeV) as an example for TRD operation. With an average number of twelve charged secondary particles we observe only tracks of electrons, which look like chains of cluster numbers in each of the eight TR chambers. There is also the "gray background", originating from relatively low energy (few GeV) secondary hadrons, which deteriorate the rejection power.

The two-dimensional analysis shown in fig. 50 has been used for π/e rejection at the trigger level. This method selects events on the scatter plot of anode versus cathode hits. (A hit means an ionization cluster

with an energy of more than 5 keV.) For the number of clusters $N \gg N_{\text{anode(cathodes)}}^{\text{threshold}}$ there is a corresponding 90% electron efficiency (fig. 50a). Fig. 50b shows pion contamination for isolated pions. In the non-isolated case of p-Be interactions (fig. 50c), the scatter plot for pions is dramatically changed owing to the presence of extra particles, which lie within the “anode-cathode strips cross” (upper right-hand part of fig. 50). These particles produce a lot of uncorrelated hits into the two-dimensional plot and therefore increase the number of faked electrons. This is the main reason why the rejection power deteriorates for non-isolated particles (fig. 51). In fact, it results from misidentification not only for a single pion, but also for 2π , 3π , $\pi + \gamma$ -conversion, heavy ionizing particles etc., which pass inside the same anode (cathode) strip and simulate an electron candidate. As a result, the rejection power of the TRD for high multiplicity becomes worse (figs. 48 and 50). Nevertheless, the rejection power of the HELIOS TRD for a high density of secondaries is 2.5×10^{-2} , which allows for a clean enough sample of non-isolated electrons (fig. 52).

There are at least two ways of achieving a better TRD rejection power under high multiplicity conditions:

1) By avoiding extra particles with the aid of a pixel-like structure of the TRD – a difficult and quite expensive method;

2) The control of extra particles (see fig. 50d) by measuring both dE/dx and TR X-rays for each TRD chamber channel. This approach will be considered in more detail in the next section.

6. TRDs for future high energy and high luminosity colliders: possibilities and limitations

Experiments at future hadron colliders open up a new domain of phenomena at the TeV-energy scale and the relevant particles are quarks, fragmentation into jets and leptons. The energies of these final-state particles lie in the region of tens to hundreds of GeV, and the Lorentz factors $\gamma = E/mc^2$ range between 10 and 10^3 (for hadrons and muons) and between 10^4 and 10^5 (for electrons).

It is most probable, that many interesting physics questions will be mainly accessible through the study of leptonic channels (e , μ , ν), and efficient lepton identification over a large solid angle will be essential.

6.1. The TRD for identification of the Lorentz-factor at high particle energies

The dependence of the TR yields on $\gamma = E/mc^2$ has a threshold behavior (see figs. 20 and 38), and responds well in the TeV energy domain to tracks of high γ

($> 10^3$) particles. Therefore, the TRD for high energy electrons, muons and hadrons can be used as a tracker, operating under the condition that the high intensity soft particle background stays well under the TR threshold (like fig. 49), and is therefore almost invisible.

The main task of a TRD at a high energy collider is to provide rejection against fake electrons which arise from pathological jet fragmentation and which can simulate an isolated electromagnetic shower in a calorimeter matched to a reconstructed charged track. At very high luminosities ($> 10^{34} \text{ cm}^{-2} \text{ s}^{-1}$) the pile-up of energy from the many simultaneous interactions within even the same bunch crossing will limit the precision on the electromagnetic shower position, from the calorimeter measurements, to approximately $\sigma = 5 \text{ mm}$ [89]).

The dominant contributions to this background [71] are:

- overlaps of an energetic photon from meson decays and a charged particle from a QCD jet;
- energetic charged hadrons, that shower early in the electromagnetic calorimeter;
- electron pairs arising from π^0 and η Dalitz decays;
- accidental overlap of a prompt energetic photon with a charged hadron from the spectator particles (underlying events).

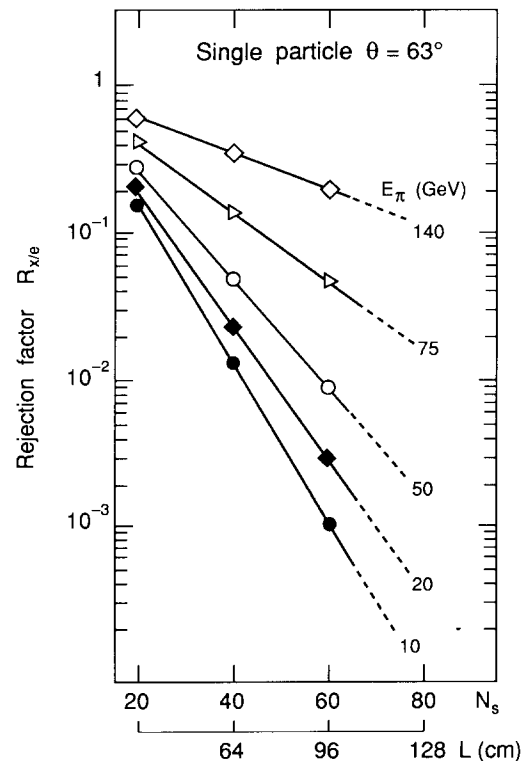


Fig. 54. Measured pion rejection as a function of the number of straws (N_s) crossed for different pion momenta.

Another important goal of the TRD is to tag high energy muons (> 100 GeV) inside jets among the relatively low momentum hadrons and to link it with the corresponding track in the muon spectrometer. The expected hadron rejection factor for 90% muon acceptance is about 10^{-1} to 10^{-2} .

6.2. The conceptual design and performance of the TRD/tracker

We discussed already (see section 4.5) the approach to achieve the best electron/pion discrimination by using many thin radiators, and many modules, which provide frequent measurements of TR photons [35]. The application of this concept to collider detectors has been discussed in ref. [90] and was described in detail in ref. [71]; this TRD/tracker is based on the "straw design" (fig. 55) where straw proportional counters are embedded in polyethylene foam serving as TR radiator [83]. For a straw diameter of 4 mm, the total drift time of the electrons is less than 40 ns (for Xe/CO₂ or Xe/CF₄ mixtures, see fig. 31); under these conditions the mean occupancy by hits from minimum

bias events for $2 \times 10^{34} \text{ cm}^{-2} \text{ s}^{-1}$ luminosity is $\approx 20\%$ [71]. The occupancy for TR X-rays is of course much lower (two percent of the charged particle occupancy).

Fig. 53 shows the electron identification (against π , 2π , 3π and γ -conversions into e^+e^-) obtained with a TRD/tracker prototype [71], containing 180 straws in a test beam. Three different threshold levels for detection from each straw have been chosen: the first threshold (TH1 at 0.2 keV) gives about 90% efficiency for MIP particles; the second threshold (TH2 at ≈ 1.5 keV) is dislocated to between one and two MIP energy losses, and the third threshold (TH3 at 4.5 keV) corresponds to $\approx 90\%$ efficiency for TR X-rays. The abscissa of each scatter plot in fig. 53 indicates, for a given particle, the number of straws where the energy deposition is above TH3; the ordinate shows the number of straws with energy deposition between TH1 and TH2. As a result, fig. 54 indicates the rejection power for pions in the range between 10 and 140 GeV, measured for isolated particles as a function of the TRD length.

The tracking capability of the TRD tracker prototype is indicated in fig. 55, showing the accuracy of the

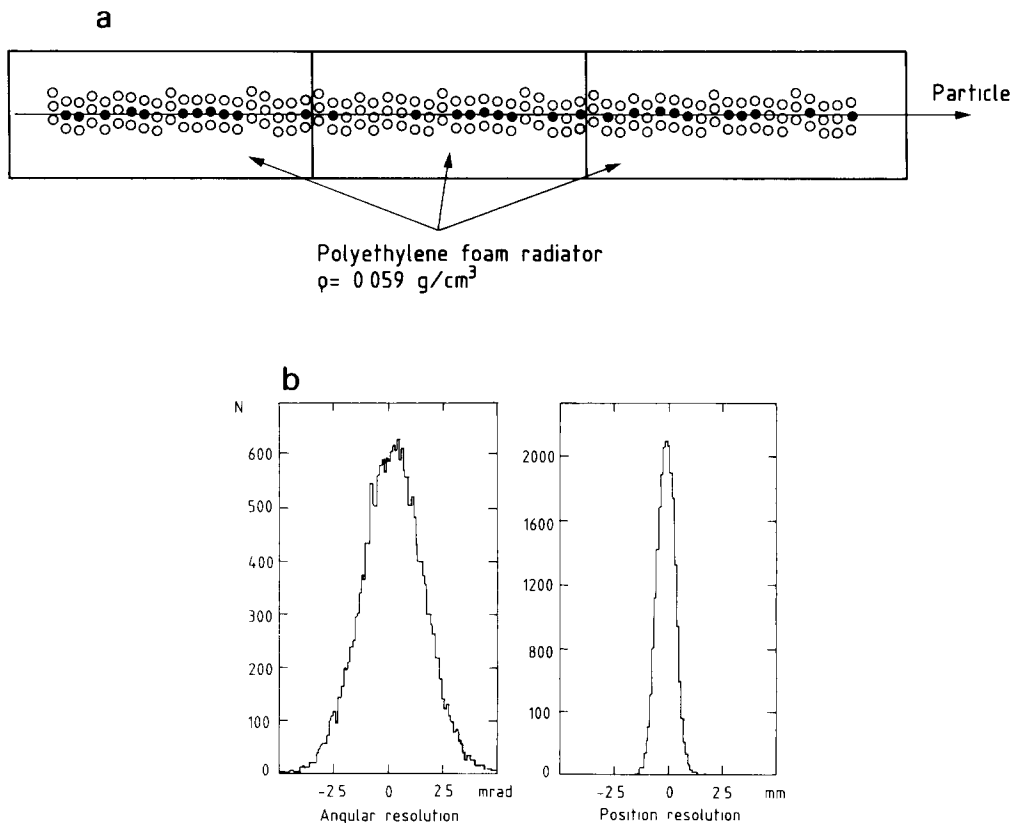


Fig. 55. (a) display of a raw event from the prototype test with 180 straws; (b) the angle and position resolution of this prototype. On average a particle crossed thirty straws.

track reconstruction for isolated particles, traversing on average 30 straws ($\sigma_x = \pm 0.4$ mm, $\sigma_\theta = \pm 1.5$ mrad).

The electron identification potential of the proposed TRD tracker was studied [71] by MC simulations for the conditions of high charged particle multiplicity. As an example the event was generated in which a 25 GeV electron and a background of 30 minimum-bias

events were superimposed. Such an event, as recorded in a TRD section, is shown in fig. 56a (all hits with energy above TH1 = 0.2 keV are shown) and in fig. 56b (hits exceeding TH3 = 5 keV).

Therefore, the simultaneous measurements of TR X-rays and dE/dx energy depositions, with straw tubes embedded in CH_2 -foam, achieve a good rejection of

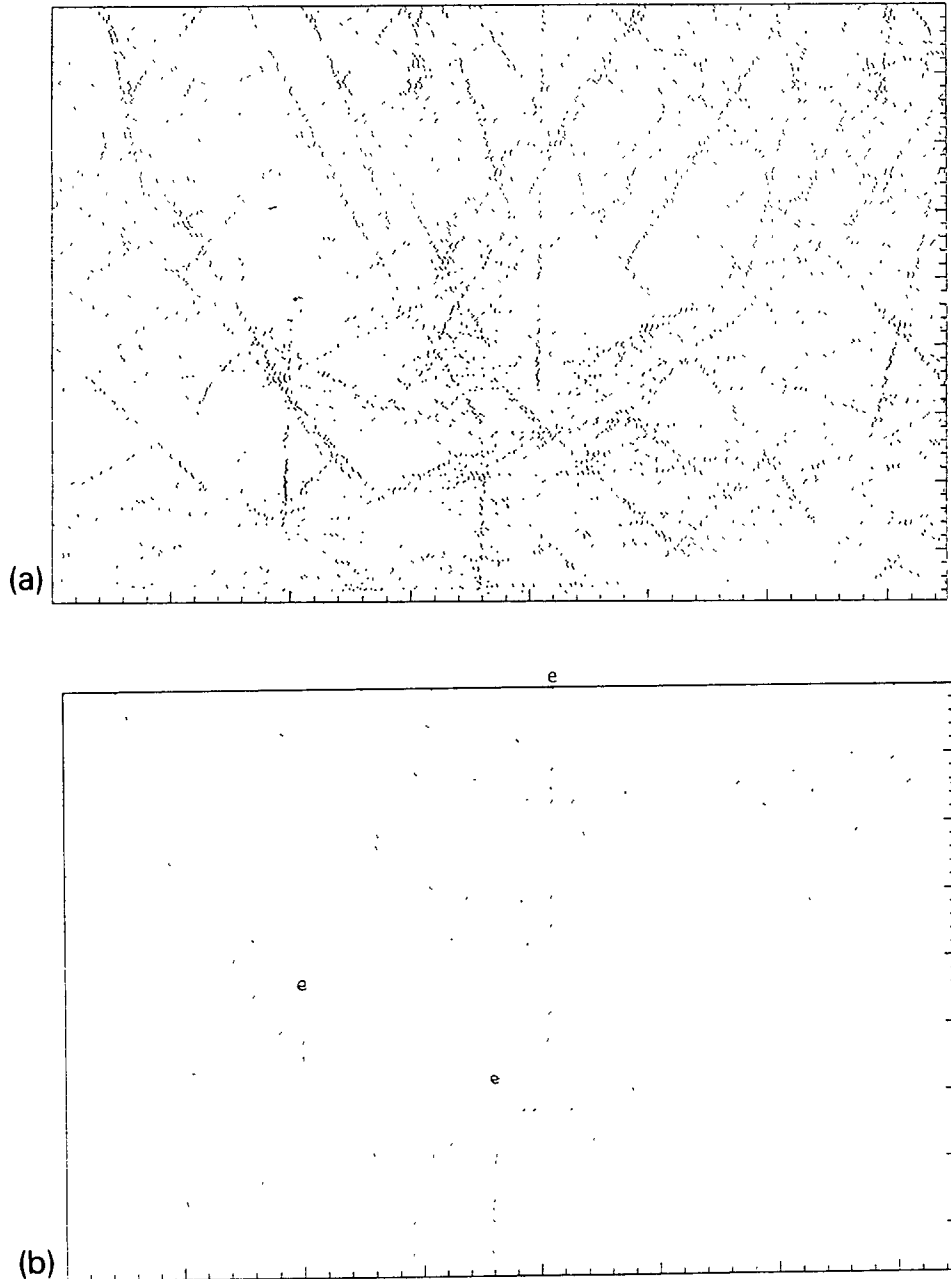


Fig. 56. Display of a simulated event in a section of the TRD/tracker operated at $L = 2 \times 10^{34} \text{ m}^{-2} \text{ s}^{-1}$. In (a) all hits exceeding TH1 are displayed. Hits above TH3 are shown in (b).

pions and converted gammas. At the same time they provide a good possibility for tracking [71].

6.3. The possibilities of the TRD for muon energy measurements

As mentioned in section 2.2. there is a saturation of X-ray yield above a certain $\gamma = E/mc^2$ value due to interference effects. Therefore, it becomes difficult to use TR yield measurements for γ -determination, which indicates the energy of particles with known mass. Of course, the saturation energy can be varied by changing the radiator parameters. However, because the formation zone between the radiator foils grows very rapidly ($\approx \gamma^2$), the value of γ -saturation cannot be increased significantly. Nevertheless, there are some efforts to measure the Lorentz factor for muons between a $\gamma_{\text{threshold}} \approx 1000$ and a $\gamma_{\text{saturation}} \approx 5000$ [91]. Using a sufficient number of TRD modules one can evaluate the energy of known mass particles (muons) in the range of a few hundred GeV.

The γ -dependence of the TR yield for 6 m long TRD is shown as an example in fig. 20 for different configuration of the TR radiator. Unfortunately, the increase of $\gamma_{\text{saturation}}$ is accompanied by a strong drop of the TR yield for the fixed total length, and therefore the statistical accuracy of energy measurements is poor. Fig. 57 shows the expected accuracy of muon energy measurements by means of a TRD with a length of 6 m. Due to the shape of the saturation curve (fig. 20) the energy error bars have to be asymmetric; fig. 57 shows the averaged error bars. According to this figure, the energy measurements by TRD do not look very promising.

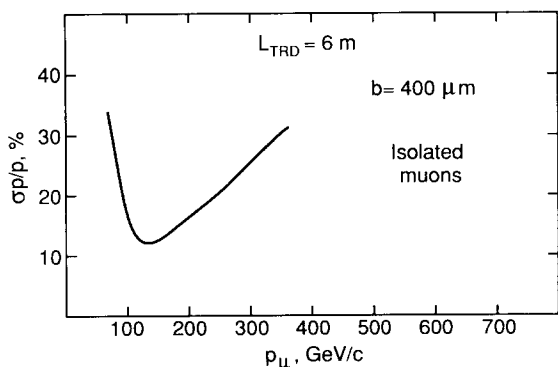


Fig. 57. The expected (optimistic) accuracy of muon energy or Lorentz-factor measurement by the TRD with a total of length 6 m; the asymmetric error bars are averaged.

7. Summary and conclusions

Fundamental agreement between experimental results and theoretical predictions was attained in many investigations of TR. We are convinced that we understand the physics phenomena of TR. Many TRDs are operated, constructed and designed for many specific purposes, including the proposals for their applications in the future.

The detection of particles by TR gives no problems anymore. The development of a still better TR detection system for high energy experiments is now the major goal. Track reconstruction within an event with multiple tracks together with identification of electrons or high γ muons (TRD/tracker concept) is a very important combination. This would improve the qualities for the detectors at high energy and high luminosity colliders. Finally, we have obtained a great deal of useful information on the design of TR detectors. It is very important, especially for large scale high energy experiments, that TRD systems can be constructed rather economically compared to many other equipment in high energy physics.

Therefore, the possibility of further extensive applications of TRD to the development of particle identification is very encouraging.

Acknowledgements

I wish to express my thanks to my colleagues and friends V. Chernjatin, I. Gavrilenko, P. Nevski, M. Potekhin, S. Smirnov, V. Sosnovtzev and A. Romanyuk for the great help; I am very grateful to C. Fabjan, D. Froidevaux and W. Willis for many very fruitful discussions, and to H. Leutz for his hard editor work.

References

- [1] V.L. Ginzburg and I.M. Frank, Zh. Eksp. Teor. Fiz. 16 (1946) 15.
- [2] P. Goldsmith and J.V. Jelley, Philos. Mag. 4 (1959) 836.
- [3] J. Doostens et al., Phys. Rev. Lett. 19 (1967) 541.
- [4] S. Prunster et al., Phys. Lett. 18B (1968) 47.
- [5] G.M. Garibian, Zh. Eksp. Teor. Fiz. 33 (1957) 1043 [Sov. Phys. JETP 6 (1958) 1079].
- [6] G.M. Garibian, Zh. Eksp. Teor. Fiz. 37 (1959) 527 [Sov. Phys. JETP 10 (1960) 372].
- [7] A.I. Alikhanian and F.R. Arutyunyan, Zh. Eksp. Teor. Fiz. 41 (1961) 2002 [Sov. Phys. JETP 14 (1962) 1421].
- [8] A.I. Alikhanian, Loeb Lectures, Harvard University, 1965.
- [9] F.R. Arutyunyan, K.A. Ispiryan and A.G. Oganesyan, J. Nucl. Phys. 1 (1965) 842 [Sov. J. Nucl. Phys. 1 (1965) 604].
- [10] F.R. Arutyunyan, K.A. Ispiryan, A.G. Oganesyan and A.A. Frangyan, Zh. Eksp. Teor. Phys. 52 (1967) 1121 [Sov. Phys. JETP 25 (1967) 743].

- [11] A.I. Alikhanian, K.M. Avakina, G.M. Garibian, M.P. Lorkyan and K.K. Shikhiarov, *Phys. Rev. Lett.* 25 (1970) 635.
- [12] A.I. Alikhanian, K.A. Ispirian, A.G. Oganessian and A.G. Tumanian, *Nucl. Instr. and Meth.* 89 (1970) 147; A.I. Alikhanian, S.A. Kankanian, A.G. Oganessian and A.G. Tumanian, *Phys. Rev. Lett.* 30 (1973) 109.
- [13] A.A. Frangian, F.R. Arutyunyan, G.A. Hekmian, A.A. Nasarian and G.B. Torgomian, *Phys. Lett.* 34B (1971) 227.
- [14] L.C.L. Yuan, C.L. Wang and S. Prunser, *Phys. Rev. Lett.* 23 (1969) 496.
- [15] L.C.L. Yuan, C.L. Wang, H. Uto and S. Prunster, *Phys. Lett.* 31B (1970) 603.
- [16] H. Uto, L.C.L. Yuan, G.F. Dell and C.L. Wang, *Nucl. Instr. and Meth.* 97 (1971) 389.
- [17] R.W. Edsworth, J. MacFall, P.K. MacKeown and G.B. Yodh, Technical Report No. 71-091, University of Maryland (1970).
- [18] M.L. Cherry et al., *Nucl. Instr. and Meth.* 115 (1973) 141.
- [19] J. Cobb et al., *Nucl. Instr. and Meth.* 140 (1977) 413.
- [20] I.M. Frank, *Usp. Fiz. Nauk* 75 (1961) 231; [*Sov. Phys. Usp.* 4 (1962) 740].
- [21] M.L. Ter-Mikaelian, *High Energy Electromagnetic Processes in Condensed Media* (Wiley-Interscience, New-York, 1972).
- [22] G.M. Garibian and Yan Shi, X-ray transition radiation, Erevan (1983) in Russian.
- [23] M.L. Ter-Mikaelian, *Nucl. Phys.* 24 (1961) 43; F.G. Bass and V.M. Yakovenko, *Usp. Fiz. Nauk* 86 (1965) 189.
- [24] V. Ermilova and V.A. Chechin, *Phys. Rev.* D19 (1979) 2053.
- [25] X. Artru, G.B. Yodh and G. Mennessier, *Phys. Rev.* D12 (1975) 1289.
- [26] M. Castellano et al., *Computer Phys. Commun.* 51 (1988) 431
- [27] M.L. Cherry et al., *Phys. Rev.* D10 (1974) 3594.
- [28] L. Durand, *Phys. Rev.* D11 (1975) 89.
- [29] F. Arutyunyan, K. Ispiryan and A. Oganessian, *Isvestia Akad. Nauk Fiz.* 28 (1964) 1866, in Russian.
- [30] A.I. Alikhanian et al., preprint EPhI, ME-2 (1970)
- [31] C.L. Wang et al., *Phys. Lett.* 29 (1972) 814.
- [32] C.W. Fabjan and W. Struczinski, *Phys. Lett.* 57B (1975) 483.
- [33] M.L. Cherry and D. Muller, *Phys. Rev. Lett.* 38 (1977) 5.
- [34] M.L. Cherry, *Phys. Rev.* D17 (1978) 2245.
- [35] B. Dolgoshein, *Nucl. Instr. and Meth.* A252 (1986) 137.
- [36] V. Grishin et al., Lebedev Phys. Institute preprint No. 201 (1977).
- [37] A.I. Alikhanian et al., *Nucl. Instr. and Meth.* 158 (1979) 137
- [38] M. Deutchmann et al., preprint CERN EP/80-155 (1980).
- [39] A. Denisov et al., preprint Fermilab-Conf-84/134E (1984)
- [40] C. Camps et al., *Nucl. Instr. and Meth.* 131 (1975) 411.
- [41] A.I. Alikhanian et al., *Sov. Phys. JETP* 38 (1974) 663
- [42] T.A. Prince et al., *Nucl. Instr. and Meth.* 123 (1975) 231
- [43] C.W. Fabjan, *Nucl. Instr. and Meth.* 146 (1977) 343.
- [44] T. Ludlam et al., *Nucl. Instr. and Meth.* 180 (1981) 413.
- [45] C.W. Fabjan et al., *Nucl. Instr. and Meth.* 185 (1981) 119.
- [46] B. Baushe et al., Proc. Int. Conf. on Instrumentation for Collider Beam Physics, 1982.
- [47] J.E. Bateman, *Nucl. Instr. and Meth.* 103 (1972) 565
- [48] A. Bungener et al., *Nucl. Instr. and Meth.* 214 (1983) 216.
- [49] Y. Watase et al., presented at the 1986 Wire Chamber Conference, Wien, 1986.
- [50] M. Holder and H. Suhr, *Nucl. Instr. and Meth.* A263 (1988) 319.
- [51] J.-F. Detoenf, Y. Ducros, F. Feinstein et al., *Nucl. Instr. and Meth.* A265 (1988) 157
- [52] Ph. Mangeot, Contribution to ECFA workshop on Instrumentation for High Luminosity Colliders, Barcelona, 1989.
- [53] J.M. Williams and D.A. Wroblewski, *J. Mater. Sci. Lett.* 24 (1989) 4062.
- [54] C. Fabjan, *Nucl. Instr. and Meth.* 149 (1977) 343
- [55] T.A. Prince, D. Muller, G. Hartmann and M.L. Cherry, *Nucl. Instr. and Meth.* 123 (1975) 231.
- [56] V. Chernjatn et al., Preprint CERN PPE/92-170.
- [57] H. Schonbacher, ECFA Study week on Instrumentation Technology, Barcelona, Spain, 14-21 Sept. 1989, vol. 1, p. 359
- [58] R.W. Fink et al., *Rev. Mod. Phys.* 38 (1966) 513.
- [59] W.H. McMaster et al., UCRL-50174, sec. II, Rev. 1, Lawrence Rad. Lab., Univ. of California, Livermore (1969).
- [60] K. Way (ed.), *Nuclear Data Tables*, vol. 7, no. 6 (Academic Press, New York, 1970).
- [61] K. Weber, *Nucl. Instr. and Meth.* 25 (1964) 261.
- [62] V. Ermilova et al., *Nucl. Instr. and Meth.* 145 (1977) 555.
- [63] V. Konovalov et al., in: *Elementary Particle and Atomic Nucleus*, ed. B. Dolgoshein (Atomizdat, Moscow, 1986) in Russian.
- [64] L.G.H. Huxley and R.W. Compton, *The Diffusion and Drift of electrons in Gases*, (Wiley Interscience, 1974) p. 119.
- [65] B. Dolgoshein et al., preprint CERN ep/89-161 (1989)
- [66] H. Daum et al., *Nucl. Instr. and Meth.* 152 (1978) 541
- [67] A. Peisert and F. Sauli, report CERN 84-08 (1984).
- [68] L.G. Christophorov et al., *Nucl. Instr. and Meth.* 171 (1980) 491
- [69] J. Va'vra, *Nucl. Instr. and Meth.* A252 (1986) 547.
- [70] S. Majewski et al., Proc. ECFA Study Week on Instrumentation for High-Luminosity Colliders, Barcelona, 1989 (CERN 89-10, ECFA 89-124, Geneva, 1989) vol. 1, p. 239.
- [71] V. Polychronakos et al., CERN DRDC/90-38, 1990; CERN DRDC/91-47 (1991)
- [72] Y. Watase et al., *Nucl. Instr. and Meth.* A248 (1986) 379, Y. Watase, KEK preprint 387-29 (1987).
- [73] G.D. Barr et al., preprint CERN-EP/90-62 (1990); *Nucl. Instr. and Meth.* A294 (1990) 465.
- [74] C. De Marzo et al., *Nucl. Instr. and Meth.* A253 (1987) 235.
- [75] D. Errede et al., preprint FERMILAB-Conf.-89/170E (1989).
- [76] H. Grasser et al., Proc. Vienna Wire Chamber Conference, 1989; *Nucl. Instr. and Meth.* A283 (1989) 622
- [77] A. Vacchi, *Nucl. Instr. and Meth.* A252 (1986) 498.
- [78] R. Ansari et al., *Nucl. Instr. and Meth.* A263 (1988) 51.
- [79] M. Sakuda et al., *Nucl. Instr. and Meth.* A311 (1992) 57

- [80] V. Ermilova, private communication.
- [81] H. Butt et al., Nucl. Instr. and Meth. A252 (1986) 483.
- [82] H. Weidcamp, Diplomaarbeit, Rhein-Westf. Tech. Hochschule, Aachen, 1984.
- [83] V. Bondarenko et al., Preprint CERN PPE/92-171.
- [84] C. De Marzo et al., Nucl. Instr. and Meth. A252 (1987) 235.
- [85] M. Atac et al., Nucl. Instr. and Meth. 145 (1977) 251.
- [86] H. Haggerty, Fermilab-TM-1201 (1982).
- [87] B. Dolgoshein, Talk given at the ECFA workshop on Instrumentation for High Luminosity Hadron Colliders, Barcelona, September, 1989.
- [88] H. Gordon et al., CERN SPSC/83-51, SPSC/P189 (1983).
- [89] J.P. Repellin, contribution to the ICFA calorimetry study Group for Aachen, 1990.
- [90] T. Akesson et al., Proc. Workshop on Experiments, Detectors and Experimental Areas for the Supercollider, Berkeley, 1987 (World Scientific, Singapore, 1988) p. 472; T. Akesson et al., in: The feasibility of experiments at high Luminosity at the Large Hadron Collider (CERN 88-02, Geneva, 1988) p. 31.
- [91] M. Castellano, C. De Marzo, O. Erriquez et al., Nucl. Instr. and Meth. A256 (1987) 38.